A robust Mixed Finite Element model for coupled Thermo-Hydro-Mechanical problems in unsaturated porous media

Lingai Guo, Anis A. Younes, Marwan Fahs, Hussein Hoteit

To cite this version:

Lingai Guo, Anis A. Younes, Marwan Fahs, Hussein Hoteit. A robust Mixed Finite Element model for coupled Thermo-Hydro-Mechanical problems in unsaturated porous media. Computers and Geotechnics, 2025, 185 (3), pp.107320. ⟨10.1016/j.compgeo.2025.107320⟩. ⟨hal-05364948⟩

HAL Id: hal-05364948
https://hal.science/hal-05364948v1

Submitted on 14 Nov 2025

A robust Mixed Finite Element model for coupled Thermo-Hydro-Mechanical problems in unsaturated porous media

Lingai Guo[a,b], Anis Younes[a,*], Marwan Fahs[a], Hussein Hoteit[b]

[a] Institut Terre et Environnement de Strasbourg, Université de Strasbourg, CNRS, ENGEES, UMR 7063, 5 rue René Descartes 67084 Strasbourg, France

[b] Physical Science and Engineering Division, King Abdullah University of Science and Technology (KAUST), Thuwal, Saudi Arabia

Submitted to Computers and Geotechnics

Contact author: Anis Younes

E-mail: younes@unistra.fr

ABSTRACT

Simulating Thermo-Hydro-Mechanical (THM) problems in unsaturated porous media presents significant challenges due to the high nonlinearities of the coupled processes, and the potential for numerical instabilities that may lead to unphysical oscillations in pressure, stress, and temperature solutions. The Mixed Finite Element (MFE) method, known for its accurate local mass conservation even in heterogeneous domains and on unstructured meshes, is widely used to discretize fluid flow in both saturated and unsaturated porous media. However, its application in coupled THM processes under variably saturated conditions has not been thoroughly explored. In this work, a robust MFE scheme based on the lowest order Raviart-Thomas space is developed for the fluid flow and heat transport in deformable unsaturated porous media. This method is integrated with the Crouzeix-Raviart finite element method for the displacement field. To prevent unphysical oscillations induced by the hyperbolic convection term in the heat transport equation, the MFE method is combined with an upwind edge/face centered finite volume scheme. The degrees of freedom of the developed formulation are the hydraulic head, the temperature, and the displacement vectors assigned at the mesh edges. To avoid splitting errors, the coupled THM equations are solved simultaneously using a monolithic scheme. The Method of Lines is employed to transform the partial differential equations into a system of nonlinear ordinary differential equations integrated in time with high-order methods using the DASPK time solver. The developed model is validated by comparisons against analytical and finite element solutions for the one-dimensional thermal consolidation problem. Numerical experiments are performed under saturated and unsaturated conditions to show the robustness of the developed model for the simulation of THM problems in variably saturated porous media.

Keywords:

Poroelasticity, THM, Unsaturated porous media, Richard’s equation, Mixed Finite Element method, Crouzeix-Raviart Element.

1. INTRODUCTION

In this work, we consider the thermo-hydro-mechanical (THM) problem in porous media with the elastic constitutive assumption, also called the thermo-poroelasticity problem, described by the strongly coupled process of fluid flow, heat transport, and mechanical deformation. The THM problem has numerous applications in geotechnical engineering, including the disposal of underground radioactive nuclear waste (Dupray et al., 2013), exploitation of natural gas and oil (Rutqvist et al., 2009), geothermal systems (Gao et al., 2022), and CO_2 sequestration (Taron et al., 2009). The mathematical model of the THM problem is based on Biot's theory for poroelasticity (Biot, 1941), the mass conservation of fluid, and the energy conservation of heat. In this work, THM is investigated for the variably saturated porous media where the fluid flow is highly nonlinear and ruled by the Richards equation (Richards, 1931). The obtained system of coupled partial differential equations (PDE) is challenging to solve mainly because of its high nonlinearity and numerical instabilities, which can lead to unphysical spurious oscillations in pressure, stress, and temperature solutions. Therefore, the main objective of this work is to develop a robust numerical model based on advanced numerical schemes for the solution of the obtained highly nonlinear, fully coupled, and potentially degenerated PDEs.

Different numerical schemes for the THM model have been introduced in the literature (Antonietti et al., 2023; Boal et al., 2012; Chen and Ge, 2022; Gawin et al., 1996; Khoei et al., 2012; Kim, 2018; Kolesov et al., 2014; Liu et al., 2009, 2024; Zareidarmiyan et al., 2020; Zhang and Rui, 2024). However, developing robust numerical solutions of the highly coupled THM problem is still a challenging task, especially in unsaturated conditions, due to the numerical instabilities (Both et al., 2021; Lee and Yi, 2022; Liu et al., 2009; Murad and Loula, 1994; Phillips and Wheeler, 2008, 2009; Yi, 2017; Younes et al., 2010, 2022a; Zhang et al., 2020). The oscillations in the pressure or stress field, also recognized as locking in poroelasticity and elasticity simulations, mainly occur when small time steps are employed (Murad and Loula, 1994; Phillips and Wheeler, 2009; Vermeer and Verruijt, 1981). For flow in unsaturated porous media, unphysical oscillations generally appear in the presence of sharp wetting fronts (Zha et al., 2017). For heat transport, nonphysical temperature oscillations are extensively observed in the case of advection-dominated transport due to the hyperbolic nature of the advection operator (Brooks and Hughes, 1982; Younes et al., 2022a). As a result, several factors contribute to nonphysical oscillations in THM numerical solutions, which can hinder the convergence of the highly nonlinear equation system and produce inaccurate outcomes.

Several numerical methods can be used for the discretization of the fluid flow or heat transport equations, among them the Mixed Finite Element (MFE) method is locally mass conservative and can easily handle heterogeneous domains and unstructured meshes (Younes et al., 2010). MFE has been extensively employed for flow simulation in saturated (Younes and Fontaine, 2008) and unsaturated porous media (Belfort et al., 2010, 2009; Song et al., 2018; Wang and Song, 2020; Younes et al., 2022b). The hybrid technique was proposed to decrease the number of unknowns of the MFE method by eliminating the unknown edge fluxes from the final system (Brezzi and Fortin, 1991; Chavent and Roberts, 1991). Furthermore, a lumped formulation has been developed (Younes et al., 2006; 2010) to improve the monotonicity of the MFE method and reduce the nonphysical pressure oscillations in the case of transient simulations with small time steps (Younes et al., 2010, 2006). The lumped formulation has been applied to variably saturated flow simulations and showed noticeable robustness and efficiency (Belfort et al., 2010, 2009; Younes et al., 2022b). Recently, the lumped hybrid MFE method has been combined with a novel upwind edge/face centered finite volume (FV) scheme to avoid unphysical oscillations in the case of advection-dominated transport problems (Younes et al., 2022a). The new upwind lumped hybrid MFE method guarantees the continuity of both the advective and diffusive fluxes across the element edges and maintains the time derivative continuity, which allows using high-order methods for the time integration, via the method of lines (MOL).

In poroelasticity problems, the MFE method has been used for the fluid flow and combined with several methods for elasticity, such as the continuous Galerkin method (Phillips and Wheeler, 2007a, 2007b), the least-squares approach (Korsawe and Starke, 2005; Tchonkova et al., 2008), the discontinuous Galerkin (DG) finite elements (Kraus et al., 2024; Phillips and Wheeler 2008, 2009), the Hellinger–Reissner mixed formulation (Yi, 2014), the Bernardi and Raugel element (Yi, 2017), the discontinuous finite volume method (Ruiz-Baier and Lunati, 2016; Kumar et al., 2020) and the weak Galerkin method (Sun and Rui, 2017). The combination of the MFE with the nonconforming Crouzeix-Raviart (CR) finite element method for poroelasticity problems was investigated in Yi (2013) and Hu et al. (2017) for saturated conditions and in Guo et al. (2024) for unsaturated situations. This combination was shown to be efficient since it uses fewer unknowns than the mixed-mixed four-field formulations (Korsawe and Starke, 2005; Tchonkova et al., 2008; Yi, 2014) and the discontinuous Galerkin-mixed schemes (Kraus et al., 2024; Phillips and Wheeler, 2009). Notice that the CR finite element method is locally conservative and was shown to be algebraically equivalent to the lowest-order MFE method for elliptic diffusion equations (Younes et al., 2010).

In THM problems, the MFE method has been used for both poroelasticity (Brun et al., 2020, 2019; Zhang and Rui, 2024) and poroplasticity (Song et al., 2018; Wang and Song, 2020). In thermo-poroelasticity problems with small strain, the MFE method has been employed for the discretization of the fluid flow and heat transport equations and combined with the standard Galerkin finite element method for the mechanical equation (Brun et al., 2020, 2019). Zhang and Rui (2024) used the MFE method for the fluid equation and the continuous Galerkin finite element method for both the displacement and temperature fields. Solving the coupled nonlinear PDEs can bring a heavy computational burden because of the high coupling between the flow, mechanics, and heat in thermo-poroelasticity problems. To reduce the computational cost, Zhang and Rui (2024) linearized the nonlinear convective transport term in the energy conservative equation by using the fluid flux at the previous time level. Recently, meshless methods have been implemented to study the THM behavior of large deformations in unsaturated porous media (Menon and Song, 2023).

In this work, a robust unsaturated thermo-poroelasticity model is developed using advanced spatial and temporal discretization methods. The lumped hybrid MFE method is used for the spatial discretization of the fluid flow and heat transport equations under unsaturated conditions. The nonconforming CR finite element method is employed for the discretization of the displacement field. The upwind edge/face centered FV scheme (Younes et al., 2022a) is integrated with the MFE method for the discretization of the convective term in the heat transport equation to prevent unphysical temperature oscillations appearing in advection-dominated transport. The monolithic coupling algorithm, where all the equations are solved simultaneously, is adopted to prevent splitting errors. Time discretization is performed using high-order time integration methods via the MOL which was shown to be efficient for poroelasticity problems (Guo et al., 2024).

The article is structured as follows. In section 2, we recall the mathematical model governing the coupled fluid flow, heat transport, and mechanical response in the case of variably saturated porous media. In section 3, we develop the spatial discretization of the equations based on the MFE method for the Richards equation, the upwind MFE method for the heat transport equation, and the CR method for elasticity. The coupled equations are solved in time with high-order methods using the MOL. In section 4, numerical experiments are performed to validate the developed model and investigate its robustness by comparisons against classical finite element results. Section 5 concludes the study and reviews the main findings.

2. MATHEMATICAL MODEL

The governing equations for the THM problem in variably saturated media consist of the hydraulic, heat transport, and mechanical models, outlined as follows. The mathematical model is formulated on the basis of small deformations theory and infinite mobility of the air phase, which implies that air pressure distribution is quasi-static and therefore the air pressure can be considered constant.

2.1 The hydraulic model

Taking into consideration the thermal expansion as well as the solid deformation, the mass conservation equation of the non-isothermal fluid in variably saturated media is given by (Antonietti et al., 2023; Kafle et al., 2022):

$$C_{pp}\frac{\partial H}{\partial t}-C_{pT}\frac{\partial T}{\partial t}+C_{pe}\frac{\partial \varepsilon_v}{\partial t}+\nabla.\boldsymbol{q}=q_s^f\ , \tag{1}$$

where $H=h+y$ is the hydraulic head [L], $h=\dfrac{p}{\rho_w g}$ is the pressure head [L] related to the pressure p [Pa], ρ_w is the water density [ML^{-3}], g is the gravity acceleration [LT^{-2}], y is the upward vertical coordinate [L]. $C_{pp}=\left(S_w S_s+c(h)\right)$ [L^{-1}], with $S_w=\theta/\theta_s$ is the water saturation [-], θ is the current water content [L^{3}L^{-3}], θ_s is the saturated water content [L^{3}L^{-3}], $c(h)=\partial\theta/\partial h$ is the specific moisture capacity [L^{-1}], $S_s=\rho_w g\left((\alpha-n)C_s S_w+nC_w\right)$ is the specific mass storativity related to the saturation change [L^{-1}], α is the Biot coefficient [-], n is the porosity [-], C_w is the compressibility of water [M^{-1}L^{1}T^2], C_s is that of the solid grains [M^{-1}L^{1}T^2], $C_{pT}=\alpha_m^T=(1-n)\alpha_s^T+nS_w\alpha_w^T$ is the equivalent volumetric thermal expansion coefficient [Θ^{-1}], α_s^T is the volumetric thermal expansion coefficient of the solid grain [Θ^{-1}],

α_w^T is that of the water phase [Θ^{-1}], $C_{pe} = \alpha S_w$ [-] is the volumetric expansion coefficient due to the mechanical deformation of the solid skeleton, $\varepsilon_v = \nabla \cdot \boldsymbol{u}$ is the volumetric strain, $\boldsymbol{u}$ [L] is the displacement vector, q_s^f is the source term [T^{-1}].

The primary variables in Eq. (1) are the hydraulic head of the water phase H [L], the temperature T [Θ], and the displacement vector $\boldsymbol{u}$ [L].

The Darcy fluid velocity $\boldsymbol{q}$ [LT^{-1}] is given by the Darcy's law:

$$\boldsymbol{q} = -\boldsymbol{K}\nabla H, \tag{2}$$

where $\boldsymbol{K} = \dfrac{\rho_w g}{\mu_w} k_r \boldsymbol{k}$ is the effective hydraulic conductivity tensor [LT^{-1}], k_r is the relative permeability [-], μ_w is the dynamic viscosity [ML^{-1}T^{-1}], and $\boldsymbol{k}$ is the absolute permeability tensor dependent only on the porous medium [L^2].

In this work, the water density ρ_w and the water viscosity μ_w are considered constant, as their variation with temperature can be neglected within a limited temperature range.

In unsaturated media, different constitutive models can be used for the relationships between the saturation, the relative permeability, and the pressure head (Brooks and Corey, 1966; Mualem, 1976; Van Genuchten, 1980). In relatively low-temperature conditions considered in this study, the thermal effect on the water retention curve can be neglected (Lu and McCartney, 2024). In this work, the classical van Genuchten (1980) model is adopted to approximate the saturation-pressure head relation:

$$S_e = \frac{\theta - \theta_r}{\theta_s - \theta_r} = \begin{cases} \dfrac{1}{\left(1 + \left|\alpha_v h\right|^{n_v}\right)^{m_v}} & h < 0 \\ 1 & h \geq 0 \end{cases}, \tag{3}$$

where α_v [L^{-1}] and n_v [-] are the van Genuchten parameters dependent on the porous media properties, $m_v = 1 - 1/n_v$, S_e [-] is the effective saturation and θ_r is the residual water content [L^{3}L^{-3}].

The permeability-saturation relationship is derived from the Mualem (1976) model as follows:

$$k_r = S_e^{1/2}\left[1-\left(1-S_e^{1/m_v}\right)^{m_v}\right]^2 . \tag{4}$$

The hydraulic model, given by Eqs. (1)-(4), has to be solved on the computational domain Ω of boundary $\partial\Omega$ formed by $\partial\Omega_p$ and $\partial\Omega_q$ representing, respectively, the boundary with a prescribed hydraulic head and that with a prescribed normal flux.

2.2 The heat transport model

Assuming thermal equilibrium (the same local temperature for the solid and fluid phases), the energy conservation equation in unsaturated porous media can be written as follows (Li et al., 1999; Wang and Papamichos, 1994):

$$C_{TT}\frac{\partial T}{\partial t} + \boldsymbol{q}\nabla T + \nabla.\boldsymbol{q}_d = q_s^T , \tag{5}$$

where $C_{TT} = \dfrac{(\rho C_T)_{eff}}{\rho_w C_{Tw}}$ [-], with $(\rho C_T)_{eff} = nS_w(\rho_w C_{Tw}) + (1-n)(\rho_s C_{Ts})$ the effective heat capacity for an elementary volume of the mixture of solid and fluid phases and $\rho_w C_{Tw}$, the heat capacity of the sole water phase, C_{Tw} and C_{Ts} are the specific heat capacity of the water phase and that of the solid phase [L^{2}T$^{-2}\Theta^{-1}$], ρ_s is the density of the solid phase [ML^{-3}], and q_s^T is the heat source term [T$^{-1}\Theta$].

The primary variables for the heat transport Eq. (5) are the temperature T, and the hydraulic head H since Eq. (5) involves the Darcy velocity $\boldsymbol{q}$, which is dependent on H (Eq. (2)).

The diffusive heat flux $\boldsymbol{q}_d$ in Eq. (5) is derived from the Fourrier's law (Joseph Fourier, 1878):

$$\boldsymbol{q}_d = -D\nabla T\ , \qquad (6)$$

where $D = \dfrac{k^T}{\rho_w C_{Tw}}$ is the diffusion coefficient [L^2T^{-1}], $k^T = nS_w k_w^T + (1-n)k_s^T$ is the effective thermal conductivity, k_w^T and k_s^T are the thermal conductivity of the water phase and that of the solid phase, respectively [$MLT^{-3}\Theta^{-1}$].

The heat transport model, formed by Eq. (5) and Eq. (6), is solved on the computational domain Ω of boundaries $\partial\Omega_T$ and $\partial\Omega_I$ corresponding, respectively, to the boundaries with fixed temperature and fixed heat flux.

2.3 The mechanical model

Under quasi-static conditions, the linear momentum balance equation is expressed as,

$$\nabla \cdot \boldsymbol{\sigma} + \rho_b \boldsymbol{g} = \mathbf{0}\ , \qquad (7)$$

where $\rho_b = \rho_s(1-n) + nS_w\rho_w$ is the bulk density [ML^{-3}], $\boldsymbol{\sigma}$ is the total stress tensor [$ML^{-1}T^{-2}$] which is related to the effective stress $\boldsymbol{\sigma}_e$ [$ML^{-1}T^{-2}$], the fluid pressure p, and the temperature T by:

$$\boldsymbol{\sigma} = \boldsymbol{\sigma}_e - \alpha S_w\left(p - p_{ref}\right)\mathbf{I} - \alpha_m^T K_d\left(T - T_{ref}\right)\mathbf{I}\ , \qquad (8)$$

where $\mathbf{I}$ is the identity matrix, $p = \rho_w gh$ is the water pressure [$ML^{-1}T^{-2}$], $K_d = (3\lambda + 2\mu)/3$ is the bulk modulus of the porous medium [$ML^{-1}T^{-2}$], $\lambda = \dfrac{\nu E}{(1+\nu)(1-2\nu)}$ and $\mu = \dfrac{E}{2(1+\nu)}$ are the Lamé coefficients [$ML^{-1}T^{-2}$], E is the Young's modulus [$ML^{-1}T^{-2}$], ν is the Poisson's ratio [-], p_{ref} and T_{ref} are, respectively, the pressure and the temperature reference values.

Assuming small deformations, isotropic materials, and linear stress-strain relationship, the constitutive relation between the effective stress and the displacement can be expressed using the generalized Hooke's law:

$$\boldsymbol{\sigma}_e = \mu\left(\nabla \boldsymbol{u} + \left(\nabla \boldsymbol{u}\right)^T\right) + \lambda\left(\nabla \cdot \boldsymbol{u}\right)\mathbf{I}\,. \tag{9}$$

Thus, the mechanical model requires the solution of the Eqs. (7-9) on the domain Ω of boundary $\partial\Omega$ which is formed by $\partial\Omega_u$ and $\partial\Omega_t$ corresponding, respectively, to the boundary with a prescribed displacement and prescribed traction. The primary variables of the mechanical model are the hydraulic head H, the temperature T, and the displacement vector $\boldsymbol{u}$.

In summary, the unsaturated thermo-poroelasticity problem requires the solution of the coupled equations of the fluid flow (Eqs. (1-4)), of the heat transport (Eqs. (5-6)), and of the poroelasticity (Eqs (7-9)) with the boundary conditions specified for each physics. It is noticeable that the Dirichlet and Neumann boundaries are specified for each physics sufficiently and uniquely for all the boundary edges of the investigated domain so that the following criterions always hold: $\partial\Omega_p \cup \partial\Omega_q = \partial\Omega$ and $\partial\Omega_p \cap \partial\Omega_q = 0$ for the hydraulic model, $\partial\Omega_T \cup \partial\Omega_I = \partial\Omega$ and $\partial\Omega_T \cap \partial\Omega_I = 0$ for the heat transport model, $\partial\Omega_u \cup \partial\Omega_t = \partial\Omega$ and $\partial\Omega_u \cap \partial\Omega_t = 0$ at each dimension for the mechanical model.

3. DISCRETIZATION

In the following, the MOL is used for the discretization of the coupled thermo-hydro-mechanical equations with the corresponding initial and boundary conditions. To this aim, the coupled equations are discretized in space on general triangular meshes with the lumped hybrid MFE and the CR finite element methods. Then, the obtained nonlinear system of ODEs is discretized in time with high-order time integration methods. The main stages for the discretization of the governing equations are summarized in the next subsections.

3.1 Discretization of the fluid flow equations

Using the lowest-order MFE method, the Darcy velocity inside a triangular element E is approximated with the lowest-order Raviart-Thomas (RT) vectorial basis functions (Raviart and Thomas, 1977):

$$\boldsymbol{q}^E = \sum_{i=1,3} Q_i^E \boldsymbol{w}_i^E \,, \tag{10}$$

where $\boldsymbol{w}_i^E = \dfrac{1}{2|E|}\begin{pmatrix} x - x_i^E \\ y - y_i^E \end{pmatrix}$ is the RT basis function, $|E|$ is the area of the element E, $\left(x_i^E, y_i^E\right)$ is the vertex coordinate opposite to the edge i (see Fig. 1), $Q_i^E = \int_i \boldsymbol{q}^E . \boldsymbol{\eta}_i^E$ is the water flux across the edge i of E, $\boldsymbol{\eta}_i^E$ is the outward unit normal vector to the edge i.

The lumped formulation of the MFE method (Younes et al., 2006) is elaborated in two steps. In the first step, the stationary flux $\bar{Q}_i^E$ at the edge i of the element E is obtained from the variational formulation of Eq. (10) on E for the steady-state mass conservation Eq. (1), leading to (see Younes et al., 2006):

$$\bar{Q}_i^E = \sum_{j=1,3} \left(\frac{\alpha_{K,i}^E \alpha_{K,j}^E}{\alpha_K^E} - B_{K,ij}^{-1} \right) H_j^E \,, \tag{11}$$

where $\bar{Q}_i^E$ is the flux across the edge i in the case of a stationary problem without sink/source terms, H_j^E is the hydraulic head at the edge j, $\boldsymbol{B}_K^E$ is the elemental matrix of terms $B_{K,ij} = \int_E \boldsymbol{K}_E^{-1} \boldsymbol{w}_i^E \boldsymbol{w}_j^E$, $\boldsymbol{K}_E$ is the effective hydraulic conductivity tensor associated to the element E, $\alpha_{K,i}^E = \sum_{j=1,3} B_{K,ij}^{-1}$ and $\alpha_K^E = \sum_{i=1,3} \alpha_{K,i}^E$.

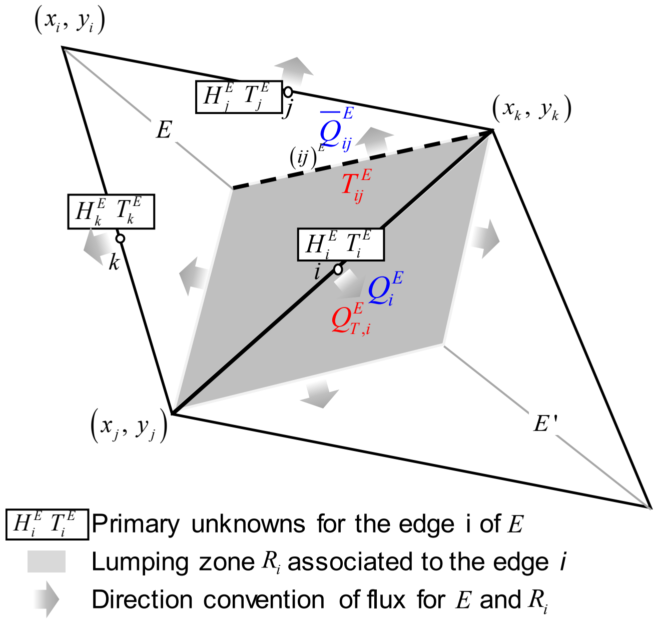

Figure 1: The denotations of lumped hybrid MFE method for fluid and heat flux discretization.

In the second step, a lumping region R_i (grey region in Fig.1) is assigned to each edge i, by joining the centers of the two sharing elements E and E' with the two nodes j and k of the edge i. The area of the lumping region R_i is therefore $\frac{|E|}{3}+\frac{|E'|}{3}$. The integration of the mass conservation Eq. (1) over R_i gives (see Fig.1 for notations):

$$\left\{C_{pp}^E \frac{|E|}{3}\frac{\partial H_i^E}{\partial t} - C_{pT}^E \frac{|E|}{3}\frac{\partial T_i^E}{\partial t} + C_{pe}^E \frac{|E|}{3}\frac{\partial \varepsilon_v^E}{\partial t} + \overline{Q}_{ij}^E + \overline{Q}_{ik}^E - \frac{Q_s^{f,E}}{3}\right\} + \{\ \}' = 0, \tag{12}$$

where ε_v^E is the volumetric strain at the element E, $Q_s^{f,E} = q_s^f |E|$ is the total amount of pumped/injected water in E, H_i^E and T_i^E are respectively the hydraulic head and temperature of the edge i which are associated with the lumping region R_i, $\overline{Q}_{ij}^E$ is the steady state water flux at the interior interface $(ij)^E$ between the edges i and j, calculated by integration $\overline{Q}_{ij}^E = \int_{e_{ij}} \boldsymbol{q}^E \boldsymbol{n}_{ij} = \frac{1}{3}\left(Q_j^E - Q_i^E\right)$. The shortcut $\{\ \}'$ designates the same contribution as $\{\ \}$, but of the adjacent element E'. Using the steady-state mass balance at the element E $\left(\overline{Q}_{ij}^{E}+\overline{Q}_{ik}^{E}+\overline{Q}_{i}^{E}=0\right)$ and Eq. (11), the mass conservation in the lumping region R_i yields:

$$\left\{C_{pp}^{E}\frac{|E|}{3}\frac{\partial H_i^E}{\partial t}-C_{pT}^{E}\frac{|E|}{3}\frac{\partial T_i^E}{\partial t}+C_{pe}^{E}\frac{|E|}{3}\frac{\partial \varepsilon_v^E}{\partial t}+\sum_{j=1,3}\left(B_{K,ij}^{-1}-\frac{\alpha_{K,i}^{E}\alpha_{K,j}^{E}}{\alpha_K^E}\right)H_j^E-\frac{Q_s^{f,E}}{3}\right\}+\{\ \}'=0 \quad (13)$$

The final hydraulic system is obtained by writing Eq. (13) for all mesh edges, except for those of the boundary $\partial\Omega_p$ with a prescribed head. Notice that the lumped formulation Eq. (13) has an improved monotonicity compared to the standard MFE method (Younes et al., 2006). Furthermore, the time derivative in Eq. (13) remains in its continuous form (contrarily to the standard MFE formulation) which allows the use of the MOL (Younes et al., 2006).

3.2 Discretization of the heat transport equation

The new upwind lumped hybrid MFE scheme proposed in Younes et al., (2022a) ensures oscillation-free solutions by combining the lumped formulation of the hybrid MFE discretization with the upwind edge-centered FV method, without any approximation for the upwind variables. Thus, for a given lumping region, the advection flux at one of its interfaces is evaluated using the variables from that lumping region (in the case of outflow) or from its adjacent lumping region (in the case of inflow). The scheme of Younes et al., (2022a) is extended in this study for the discretization of the energy conservation equation.

Like the Darcy flux, the diffusive flux, given by Eq. (6), is approximated with the lowest-order RT elements as:

$$\boldsymbol{q}_d^E=\sum_{i=1,3}Q_{d,i}^E\boldsymbol{w}_i^E\,. \quad (14)$$

As previously, the first step of the lumped MFE formulation gives the steady-state dispersive flux (similarly to the Darcy flux in Eq. (11)) as follows:

$$\overline{Q}_{d,i}^{E}=\sum_{j=1,3}\left(\frac{\alpha_{D,i}^{E}\alpha_{D,j}^{E}}{\alpha_D^E}-B_{D,ij}^{-1}\right)T_j^E\,, \quad (15)$$

where D_E is the diffusion coefficient in the element E, $B_{D,ij} = \int_E D_E^{-1} \boldsymbol{w}_i^E \boldsymbol{w}_j^E$, $\alpha_{D,i}^E = \sum_{j=1,3} B_{D,ij}^{-1}$, and $\alpha_D^E = \sum_{i=1,3} \alpha_{D,i}^E$.

In the second step, the integration of the heat transport Eq. (5) over the lumping region R_i writes (see Younes et al., 2022a):

$$\left\{ \lambda_E \frac{\partial T_i^E}{\partial t} + Q_{ij}^E T_{ij}^E + Q_{ik}^E T_{ik}^E - T_i^E \left(Q_{ij}^E + Q_{ik}^E \right) + \overline{Q}_{d,ij}^E + \overline{Q}_{d,ik}^E - \frac{Q_s^{T,E}}{3} \right\} + \{\ \}' = 0, \tag{16}$$

where $\lambda_E = \frac{|E|\, C_{TT}^E}{3}$, $Q_{ij}^E = \frac{1}{3}\left(Q_j^E - Q_i^E \right)$ is the water flux at the interior interface $(ij)^E$ (Fig. 1), $Q_s^{T,E} = q_s^T |E|$ is the total heat source over the element E, $\overline{Q}_{d,ij}^E$ and $\overline{Q}_{d,ik}^E$ are the steady-state dispersive fluxes at the interior interfaces $(ij)^E$ and $(ik)^E$ which verify $\overline{Q}_{d,ij}^E + \overline{Q}_{d,ik}^E + \overline{Q}_{d,i}^E = 0$.

The temperature T_{ij}^E (see Fig. 1) at the interface $(ij)^E$ is the upstream temperature, defined by (Younes et al., 2022a):

$$T_{ij}^E = \tau_{ij}^E T_i^E + \left(1 - \tau_{ij}^E \right) T_j^E, \tag{17}$$

with $\tau_{ij}^E = 1$ if $Q_{ij}^E \geq 0$, else $\tau_{ij}^E = 0$.

Substituting Eq. (17) and Eq. (15) into Eq. (16), yields:

$$\left\{ \lambda_E \frac{\partial T_i^E}{\partial t} + Q_{ij}^E \left(1 - \tau_{ij}^E \right) \left(T_j^E - T_i^E \right) + Q_{ik}^E \left(1 - \tau_{ik}^E \right) \left(T_k^E - T_i^E \right) + \sum_{j=1,3} \left(B_{D,ij}^{-1} - \frac{\alpha_{D,i}^E \alpha_{D,j}^E}{\alpha_D^E} \right) T_j^E - \frac{Q_s^{T,E}}{3} \right\} + \{\ \}' = 0 \tag{18}$$

The final heat transport system to solve is therefore given by writing Eq. (18) for all mesh edges except those at the boundary $\partial\Omega_T$ with a prescribed temperature.

3.3 Discretization of the mechanical model

The CR method is used hereafter for the discretization of the mechanical model. The displacement vector $\boldsymbol{u}^E$ over the element E is approximated by (Fig. 2):

$$\boldsymbol{u}^E = \sum_{i=1,3} \boldsymbol{u}_i^E \varphi_i^E \tag{19}$$

where φ_i^E is the interpolation function related to the edge i, varying linearly from 1 at the edge i to -1 at the opposite node i and intersecting the two edges j and k at their centers (Fig.2). For an interior edge i sharing two adjacent elements E and E', the interpolation function φ_i, associated to the edge i, is the union $\varphi_i = \varphi_i^E \cup \varphi_i^{E'}$. The interpolation function degenerates to $\varphi_i = \varphi_i^E$ for a boundary edge.

Using Eq. (19), the volumetric strain at the element E becomes:

$$\varepsilon_v^E = \nabla \cdot \boldsymbol{u}^E = \sum_{i=1,3} \left(u_{i,x}^E \frac{\Delta y_i^E}{|E|} + u_{i,y}^E \frac{\Delta x_i^E}{|E|} \right), \tag{20}$$

where $\Delta x_i^E = x_j^E - x_k^E$ and $\Delta y_i^E = y_k^E - y_j^E$.

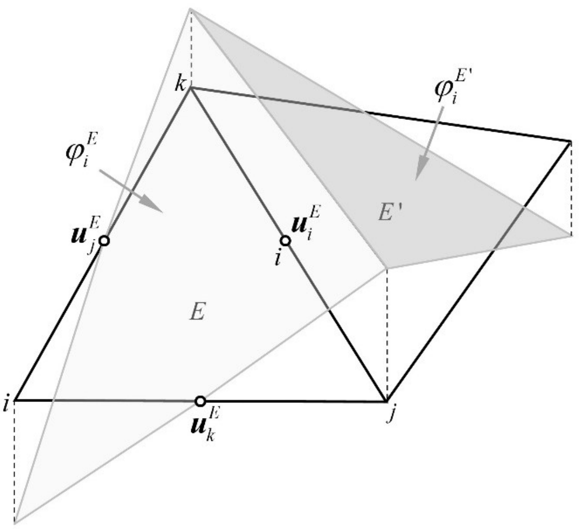

Figure 2: The interpolation function φ_i of the nonconforming CR finite element.

The weak formulation of the equilibrium Eq. (7) over the domain Ω, using the test function φ_i and Green's formula writes:

$$\int_{\Omega} \boldsymbol{\sigma}\cdot\nabla\varphi_i - \int_{\partial\Omega} \varphi_i \boldsymbol{\sigma}\cdot\boldsymbol{\eta}_{\partial\Omega} = \int_{\Omega} \rho_b \boldsymbol{g}\varphi_i \, , \tag{21}$$

where $\boldsymbol{\eta}_{\partial\Omega}$ is the outward normal unit vector to the boundary $\partial\Omega$. For an edge i of the boundary $\partial\Omega_t$, the second term of Eq. (21) corresponds to the prescribed traction $\boldsymbol{t}_i$ for the edge i. For an interior edge i, the second term vanishes, and Eq. (21) contains the contribution of the two adjacent elements E and E':

$$\begin{cases} \int_{E} \boldsymbol{\sigma}^{E}\cdot\nabla\varphi_i^{E} = \int_{E} \rho_b^{E} \boldsymbol{g}\varphi_i^{E} + \int_{i} \boldsymbol{t}_i & \text{\textit{for edges in} } \partial\Omega_t \\ \int_{E} \boldsymbol{\sigma}^{E}\cdot\nabla\varphi_i^{E} + \int_{E'} \boldsymbol{\sigma}^{E'}\cdot\nabla\varphi_i^{E'} = \int_{E} \rho_b^{E} \boldsymbol{g}\varphi_i^{E} + \int_{E'} \rho_b^{E'} \boldsymbol{g}\varphi_i^{E'} & \text{\textit{for interior edges}} \end{cases} \tag{22}$$

Substituting Eqs. (8-9) and (19) into Eq. (22) yields the two equations to solve (for the displacement in the horizontal and vertical directions) for an arbitrary edge i:

$$\begin{aligned} &\left\{ \sum_{j=1,3} N_{E,ij}^{1} u_{j,x}^{E} + \sum_{j=1,3} N_{E,ij}^{2} u_{j,y}^{E} + s_{pT}^{E}\Delta y_i^{E} \right\} + \left\{\ \right\}' = L_i t_i^{x} \\ &\left\{ \sum_{j=1,3} N_{E,ij}^{3} u_{j,x}^{E} + \sum_{j=1,3} N_{E,ij}^{4} u_{j,y}^{E} + s_{pT}^{E}\Delta x_i^{E} \right\} + \left\{\ \right\}' = \left(\rho_b^{E} \frac{|E|}{3} + \rho_b^{E'} \frac{|E'|}{3} \right) g + L_i t_i^{y} \end{aligned} \tag{23}$$

where $s_{pT}^{E} = -\frac{\beta_p^{E}}{3} \sum_{j=1,3} \left(H_j^{E} - \bar{y}_j - H_{ref} \right) - \frac{\beta_T^{E}}{3} \sum_{j=1,3} \left(T_j^{E} - T_{ref} \right)$ is related to the pore pressure and the temperature with $\bar{y}_j$ denoting the elevation of the edge j in the element E, $\beta_p^{E} = \alpha^{E} S_w^{E} \rho_w g$ and $\beta_T^{E} = \alpha_m^{T,E} K_d^{E}$. $\boldsymbol{t}_i = \left(t_i^{x}, t_i^{y} \right)$ is the prescribed traction at the boundary edge i of length L_i and $\left\{\ \right\}'$ denotes the same term as in the first curly bracket but for the neighbor element E'. The four local matrices in Eq. (23) are defined as follows:

$$
\begin{aligned}
N_{E,ij}^{1} &= \frac{2\mu_E+\lambda_E}{|E|}\Delta y_i^E \Delta y_j^E + \frac{\mu_E}{|E|}\Delta x_i^E \Delta x_j^E \\
N_{E,ij}^{2} &= \frac{\mu_E}{|E|}\Delta x_i^E \Delta y_j^E + \frac{\lambda_E}{|E|}\Delta y_i^E \Delta x_j^E \\
N_{E,ij}^{3} &= \frac{\mu_E}{|E|}\Delta y_i^E \Delta x_j^E + \frac{\lambda_E}{|E|}\Delta x_i^E \Delta y_j^E \\
N_{E,ij}^{4} &= \frac{2\mu_E+\lambda_E}{|E|}\Delta x_i^E \Delta x_j^E + \frac{\mu_E}{|E|}\Delta y_i^E \Delta y_j^E
\end{aligned}
\tag{24}
$$

The final system is obtained by writing Eq. (23) for all mesh edges (except for those with a prescribed displacement) by implicitly imposing the continuity of the displacement vectors at the interface between the two adjacent elements E and E' $\left(\boldsymbol{u}_i = \boldsymbol{u}_i^E = \boldsymbol{u}_i^{E'}\right)$.

To stabilize the CR discretization, a penalty term is added to the variational formulation. The penalty term, developed by Hansbo and Larson (2003) using the connection between CR and DG methods, is implemented in this work (see Guo et al., 2024):

$$
Jump = 2\mu\gamma_1 \sum_{e\in\Lambda} L_e^{-1} \int_e \boldsymbol{u}\;_{e}\;\; \varphi_i\;_{e} , \tag{25}
$$

where γ_1 is the penalty parameter that can be fixed to 0.5 (Hu et al., 2017). All the edges e in the investigated domain Ω constitute the set Λ. L_e is the length of the edge e. The jump of a function $\boldsymbol{w}(x)$ (vector or scalar-valued) across the edge e shared by the two adjacent elements E and E' is defined as $\boldsymbol{w}\;_{e}(x) = \boldsymbol{w}_E(x) - \boldsymbol{w}_{E'}(x),\ x \in e$.

3.4 Coupling Scheme

The final spatially discretized equations of the three-field problem are given by the coupled Eqs. (13), (18), and (23). The obtained system of nonlinear equations is solved using a monolithic scheme, written as:

$$\begin{bmatrix} \mathbf{C}_{HH}^{T} & \mathbf{C}_{TH}^{T} & \mathbf{C}_{MH}^{T} \\ \mathbf{0} & \mathbf{C}_{TT}^{T} & \mathbf{0} \\ \mathbf{0} & \mathbf{0} & \mathbf{C}_{MM}^{T} \end{bmatrix} \begin{Bmatrix} \dfrac{\partial \mathbf{H}}{\partial t} \\ \dfrac{\partial \mathbf{T}}{\partial t} \\ \dfrac{\partial \mathbf{u}}{\partial t} \end{Bmatrix} + \begin{bmatrix} \mathbf{C}_{HH} & \mathbf{0} & \mathbf{0} \\ \mathbf{C}_{HT} & \mathbf{C}_{TT} & \mathbf{0} \\ \mathbf{C}_{HM} & \mathbf{C}_{TM} & \mathbf{C}_{MM} \end{bmatrix} \begin{Bmatrix} \mathbf{H} \\ \mathbf{T} \\ \mathbf{u} \end{Bmatrix} + \begin{Bmatrix} \mathbf{Q}_{\mathbf{f}} \\ \mathbf{Q}_{\mathbf{T}} \\ \mathbf{Q}_{\mathbf{m}} \end{Bmatrix} = \mathbf{0} , \qquad (26)$$

where $\{\mathbf{H} \quad \mathbf{T} \quad \mathbf{u}\}^{T}$ is the primary unknowns vector formed by the hydraulic head, the temperature, and the displacement components at each direction for all the edges (except for Dirichlet boundary edges) and $\left\{\dfrac{\partial \mathbf{H}}{\partial t} \quad \dfrac{\partial \mathbf{T}}{\partial t} \quad \dfrac{\partial \mathbf{u}}{\partial t}\right\}^{T}$ is the corresponding time derivatives. Therefore, there are four degrees of freedom in total at each edge center. $\{\mathbf{Q}_{\mathbf{f}} \quad \mathbf{Q}_{\mathbf{T}} \quad \mathbf{Q}_{\mathbf{m}}\}^{T}$ are the other constant terms in the discretization equations. The matrices $\mathbf{C}_{HH}^{T}$, $\mathbf{C}_{TH}^{T}$, $\mathbf{C}_{MH}^{T}$, $\mathbf{C}_{TT}^{T}$, $\mathbf{C}_{MM}^{T}$, $\mathbf{C}_{HH}$, $\mathbf{C}_{TT}$, $\mathbf{C}_{HM}$, $\mathbf{C}_{TM}$, $\mathbf{C}_{MM}$ are the stiffness matrices. Notice that $\mathbf{C}_{MM}^{T}$ is a fictitious diagonal matrix, added to enhance the convergence of the ODE solver. In this work, the diagonal terms of $\mathbf{C}_{MM}^{T}$ are fixed to a small value $\left(10^{-7}\right)$. The calculation details of the matrices in Eq. (26) are listed in the appendix.

The equations in the system (26) are nonlinear since the stiffness matrices are dependent on the solution $\{\mathbf{H} \quad \mathbf{T} \quad \mathbf{u}\}^{T}$. The final nonlinear system Eq. (26) is solved in time with the DASPK solver. This solver uses high-order time integration methods which are more efficient than low-order methods for solving challenging unsaturated flow problems (Tocci et al., 1997). The Fixed Leading Coefficient Backward Difference Formula (FLCBDF) is employed in DASPK with variable order (up to the 5th). The Newton-Raphson method is used for the linearization of the obtained system with a Jacobian matrix J approximated by the finite difference method. Three techniques are used to improve the efficiency of the solution:

(i) The same J is reused for many time steps and is updated only when the time solver fails. Indeed, when solving the nonlinear problem, the evaluation of the Jacobian matrix at each

iteration can be expensive. Reusing the Jacobian matrix can result in significant computational savings but reduces the convergence rate of the nonlinear solver from quadratic to superlinear.

(ii) The Jacobian matrix is approximated numerically with simple finite differences which requires the perturbation of the residual. To reduce the computational cost of the Jacobian evaluation, we take advantages of the sparsity of the Jacobian (from the system (26)). The columns of $\boldsymbol{J}$ are divided into independent groups and the perturbation is applied for each group separately. With this procedure, $\boldsymbol{J}$ is evaluated using a few number of residual evaluations which often corresponds to the largest number of non-zeros elements in a row of $\boldsymbol{J}$ (Hindmarsh, 1982).

(iii) Efficient order and time-step size selection schemes are used. During simulation, the local truncation error is estimated by comparing the result of a predictor polynomial to the result of a corrector solution, for a range of orders. The selected order of integration (between 1 and 5) is the one that requires the smallest computational effort to advance the approximate solution in time for a given allowable error. Once the order is selected, the time step size is computed based upon an efficient automatic time-stepping scheme which ensures that the local truncation error criterion is met by decreasing or increasing the time step size (Brenan et al., 1996). The error criterion is met if the truncation error is under a fixed value, which is function of a user-defined relative and absolute tolerances.

4. NUMERICAL EXPERIMENTS

In this section, the validation of the new numerical model (called MFE-THM) is investigated by comparison against the analytical solution for a thermal consolidation problem in saturated condition. Then, numerical experiments are performed to show the robustness of the new model for the simulation of THM problems under saturated and unsaturated conditions.

4.1 The one-dimensional thermal consolidation problem

The one-dimensional thermal consolidation problem is a classical thermo-poroelasticity problem widely used for the validation of THM numerical models. The coupled equations in this problem are solved analytically for saturated conditions using the Fourier transformation (Bai, 2005). The problem is solved hereafter numerically with our new MFE-THM model as well as with the COMSOL Multiphysics model, which is based on the Galerkin finite element method with linear elements for heat transport and Taylor-Hood P2-P1 elements for poroelasticity.

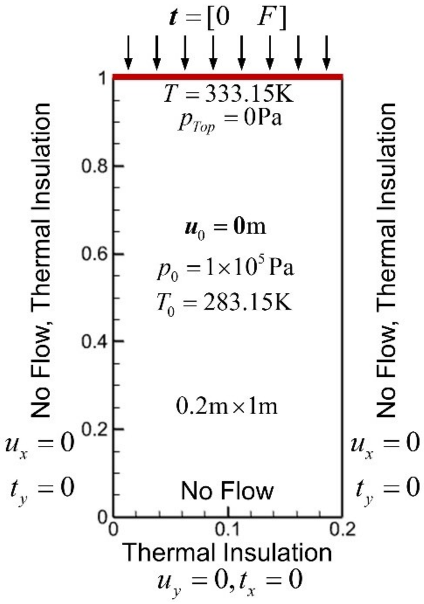

Figure 3: The configuration of the 1D thermal consolidation problem.

The configuration of the thermal consolidation problem is depicted in Fig. 3. A rectangular domain of $0.2\text{m}\times1\text{m}$ is constrained in the normal direction on the two vertical sides and the bottom. The origin of the Cartesian coordinate system is located at the bottom left corner of the domain. A uniformly distributed downward load $F = -1\times10^5\,\text{Pa}$ is applied at the top surface of the domain, where the temperature is fixed to $T_{top} = 333.15\text{K}$ and the water pressure is fixed to $p_{top} = 0\,\text{Pa}$. All the other boundaries are impermeable and thermally insulating. Initially, the domain has a uniform water pressure $p_0 = 0\,\text{Pa}$, a uniform temperature $T_0 = 283.15\text{K}$ and no deformations. Thus, the temperature interval for this test case is [283.15 333.15]K. Three observation points are chosen inside the domain with locations at (0.1, 0.1), (0.1, 0.5) and (0.1, 0.8). The computational domain is discretized into 1322 triangular elements in COMSOL with the automatic mesh generator. The same mesh is exported and used for the MFE-THM model. The iterative solver is used for both the MFE-THM and COMSOL models. A duration of 4×10^7 s is simulated. During this period, the pressure and temperature inside the domain evolve gradually from the initial state until reaching the upper boundary values at the steady state regime. The settlement increases continuously from the initial state due to the applied surface load and is affected by both pressure and temperature changes. It reaches the maximum when the steady-state regime is attained. The material parameters are listed in Table 1.

Table 1: The material properties of the one-dimensional thermal consolidation problem

Parameter	Value
Water density ρ_w	1000 [kg/m^3]
Solid density ρ_s	2600 [kg/m^3]
Porosity n	0.4
Permeability k	2.1×10^{-16} [m^2]
Water compressibility C_w	2.0×10^{-10} [Pa^{-1}]
Solid grain compressibility C_s	5.0×10^{-11} [Pa^{-1}]
Water heat conductivity k_w^T	0.5 [w/m/K]
Solid heat conductivity k_s^T	0.5 [w/m/K]
Water heat capacity C_{Tw}	4200 [J/kg/K]
Solid heat capacity C_{Ts}	800 [J/kg/K]
Water volumetric thermal expansion coefficient α_w^T	2.0×10^{-4} [1/K]
Solid volumetric thermal expansion coefficient α_s^T	1.5×10^{-5} [1/K]
Young's modulus E	6.0×10^{5} [Pa]
Poisson ratio v	0.3
Biot's coefficient α	1.0

To check the correctness of the developed MFE-THM model, simulation results are compared to the analytical solution and to COMSOL Multiphysics results. The pressure, temperature, and settlement at the three observation points are extracted and plotted in Fig. 4. The analytical solution of Bai (2005) is calculated and used as the reference. The comparisons in Fig. 4 show that both MFE-THM and COMSOL models yield similar results for the pressure, temperature, and settlement at the three observation points during the consolidation process. Furthermore, the pressure, temperature and settlement obtained numerically are in very good agreement with the analytical solution. This validates the MFE-THM model for the solution of thermo-poroelasticity problems.

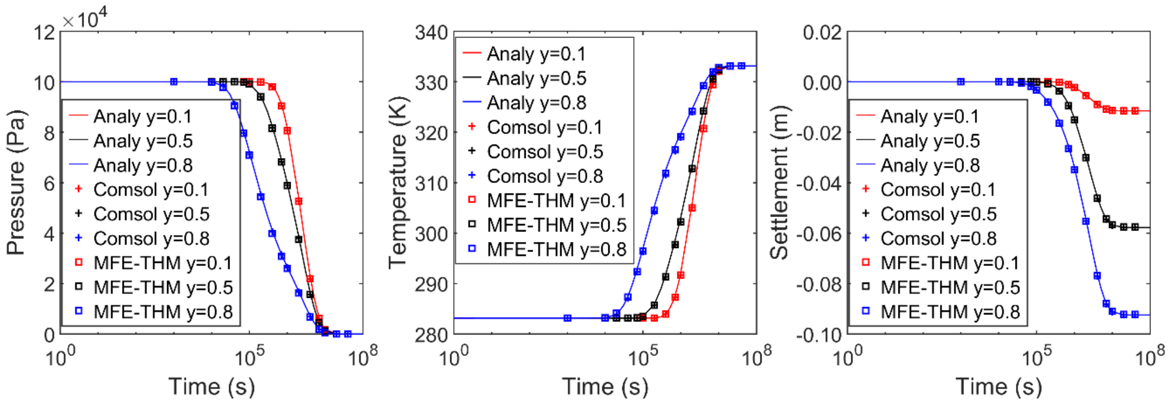

Figure 4: Results of MFE-THM and COMSOL versus the analytical solution for the thermal consolidation problem.

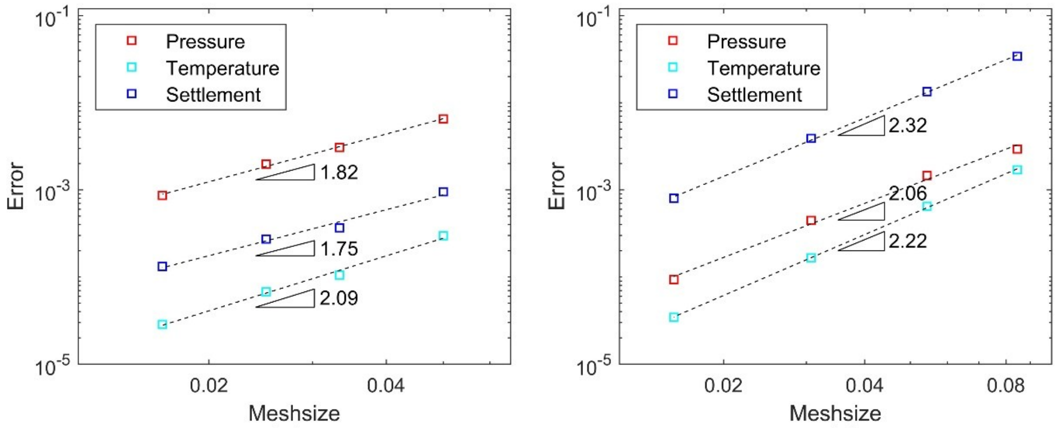

(a) (b)

Figure 5: Errors on the mean solutions of pressure, temperature, and settlement with the MFE-THM model (a) and COMSOL (b) for different mesh sizes.

A mesh convergence analysis is then performed with the MFE-THM and COMSOL models for the 1D thermal consolidation problem. To this aim, several simulations are performed with the MFE-THM model using different uniform meshes obtained by subdivision of squares into four triangles. The errors on the mean values for pressure, temperature, and settlement solutions over the domain at t = 4×10^5s are calculated by comparison against a reference solution obtained using a very fine mesh. The results of mesh convergence analysis are given in Fig. 5a for the MFE-THM model and in Fig. 5b for the COMSOL model. Results of Fig. 5 show that the solution errors depict similar convergence rates with a slope around 2.0 for both MFE-THM and COMSOL models.

Effect of the surface pressure and temperature on the settlement

To investigate the effect of the surface pressure and surface temperature on the settlement inside the column, the consolidation problem is simulated using three different top pressure values and three different surface temperatures.

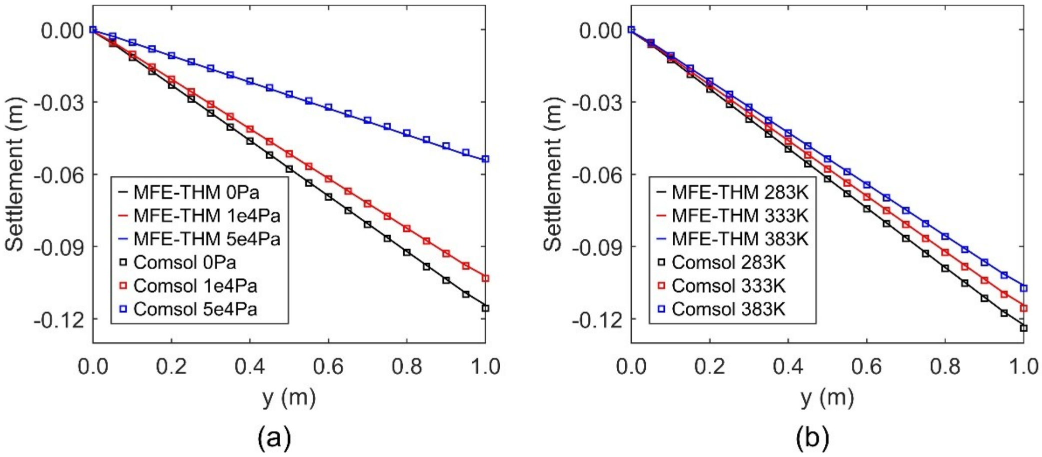

Figure 6: Settlement inside the column: effect of the surface pressure (a) and surface temperature (b).

The settlement distribution inside the column at $t = 4\times10^7$ s is calculated using the same parameters and boundary conditions as previously, but for pressure values p_{top} corresponding to 0 Pa, 1×10^4 Pa and 5×10^4 Pa. Results in Fig. 6a show that, for the three surface pressure values, the settlement varies linearly from zero (at the bottom) to its maximum value (at the top surface). The slope of the settlement curve (and therefore, the maximum settlement reached at the surface) reduces as the surface pressure increases. Good agreement is observed for the results of MFE-THM and COMSOL models in all situations. Similar behavior is observed in Fig. 6b, which shows that the settlement varies linearly for the three surface temperatures. The slope of the curve, as well as the maximum surface settlement reduce as the surface temperature increases. These results agree with the physics since the deformation due to the surface load reduces when high pressure occurs in the domain and when the temperature of the porous medium increases. The results of MFE-THM model are identical to those of the COMSOL model.

4.2 Cold water well injection problem

This problem has been suggested by Liu et al. (2009) to analyze nonphysical temperature oscillations for the saturated thermo-poroelasticity problem. In this problem, cold water is injected at a well of radius $r = 0.1\text{m}$, located at the center of an infinity reservoir. The evolution of the temperature along the radial direction is investigated at different time steps. Due to the radial symmetry of the geometry and boundary conditions, only a quarter of the domain of radius 1m is simulated (instead of the whole reservoir). The configuration of the problem is illustrated in Fig. 7.

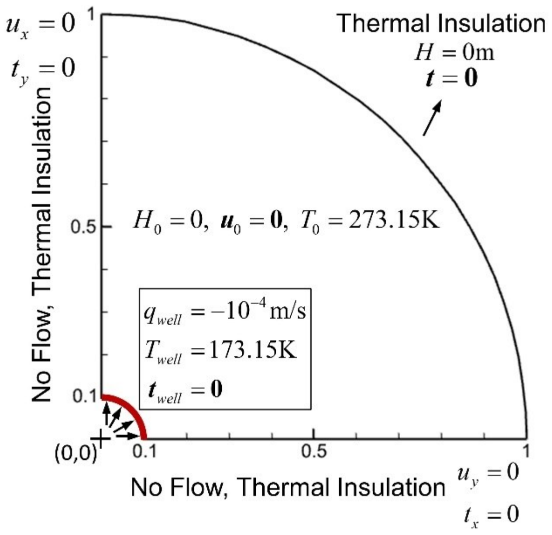

Figure 7: The configuration of the cold water well injection problem.

The horizontal and vertical boundaries are constrained in the normal direction and assumed to be impermeable and thermally insulated. Cold water of temperature $T_{well} = 173.15\mathrm{K}$ is injected from the wellbore with a prescribed flow rate $q_{well} = 10^{-4}\,\mathrm{m/s}$. Free traction boundaries are applied at the wellbore and the exterior curvilinear boundary. The latter has a prescribed zero pressure and a thermal insulation boundary condition. At the initial state, the reservoir is undeformed with a uniform zero pressure distribution and a uniform temperature distribution of $T_0 = 273.15\mathrm{K}$. Thus, the temperature interval for this problem is [173.15 273.15]K. The domain is discretized with 1634 triangular elements using a local refinement around the wellbore in COMSOL with the automatic mesh generator. The same mesh is exported and used for the MFE-THM model. The iterative solver is used for both the MFE-THM and COMSOL models. The cold water is injected during a period of $5 \times 10^4 s$. During the injection, the pressure inside the domain increases gradually until reaching a steady-state radial distribution, whereas the temperature progressively decreases inside the domain due to the transport of the cold water inside the domain by convection and conduction. The material properties for this problem are listed in Table 2.

Table 2: The material properties of the heat injection problem

Parameter	Value
Water density ρ_w	1000 [kg/m^3]
Solid density ρ_s	2600 [kg/m^3]
Porosity n	0.4
Permeability k	1.0×10^{-16} [m^2]
Water compressibility C_w	2.0×10^{-10} [Pa^{-1}]
Solid grain compressibility C_s	5.0×10^{-11} [Pa^{-1}]
Effective heat conductivity k^T	0.2/0.5/2.0 [w/m/K]
Water heat capacity C_{Tw}	4200 [J/kg/K]
Solid heat capacity C_{Ts}	800 [J/kg/K]
Water volumetric thermal expansion coefficient α_w^T	3.0×10^{-5} [1/K]
Solid volumetric thermal expansion coefficient α_s^T	3.0×10^{-5} [1/K]
Young's modulus E	3.0×10^{9} [Pa]
Poisson ratio v	0.2
Biot's coefficient α	1.0

Due to the coupling, the three fields (thermal, hydraulic, and mechanics) vary in time and space. The deformation of the porous medium is only induced by the flow and heat processes since no load is prescribed on the boundaries of the domain. To show the contribution of each field to the induced displacement, we simulate three scenarios for a duration, $t = 2\times10^4\,\mathrm{s}$. In the first scenario, the temperature of the injected water is the same as that initially occurring in the porous material, $T_{well} = T_0 = 273.15\mathrm{K}$. Thus, there is no thermal effect in this case, and the deformation of the porous material is only induced by the hydraulic process. Fig. 8a shows the final temperature distribution and the displacement field. Due to the water injection in the well, the final pressure distribution (Fig. 8b) shows a high pressure at the well boundary, which decreases progressively when moving away from the well until reaching the exterior curvilinear boundary where the pressure is fixed to zero. The pressure gradient induces radial outward

Darcy velocity (Fig.8b). Besides, the increase of the pressure inside the domain induces a deformation in the radial outward direction, as shown in Fig.8a.

In the second scenario, there is no water injection in the well ($q_{well} = 0$) and heat transport only occurs by conduction due to the lower temperature of the wellbore boundary $T_{well} = 173.15\text{K}$ compared to that initially occurring in the domain $T_0 = 273.15\text{K}$. Consequently, a small deformation occurs due to the cooling of the porous material, and a weak displacement takes place in the radial direction toward the well, reflecting the contract of the porous medium due to the cooling (Fig. 8c). The deformation itself creates an increase in pressure as we get closer to the well (Fig. 8d), thus very weak induced Darcy velocity is observed in the outward radial direction (Fig. 8d) due to the pressure gradient. The displacement and velocity magnitude are too small compared to the first scenario to show in the same scale, so a larger scale for the vector magnitude is applied in Figs. 8c-d.

The last scenario is the combination of the first and second scenarios, where the deformation is induced by both the fluid and the heat processes. Because the effect of the fluid process is much more influential than that of the heat process, the obtained deformation is very close to that of the first scenario showing a radial outward displacement field (Fig. 8e). The pressure distribution and the Darcy velocity field for the scenario 3 (Fig. 8e) are weakly affected by the heat process as the results are very close to that of scenario 1 (Fig. 8b). The temperature distribution for the last scenario (Fig. 8e) shows the propagation of the radial cooling front from the well to the further end, due to heat transport by advection and conduction.

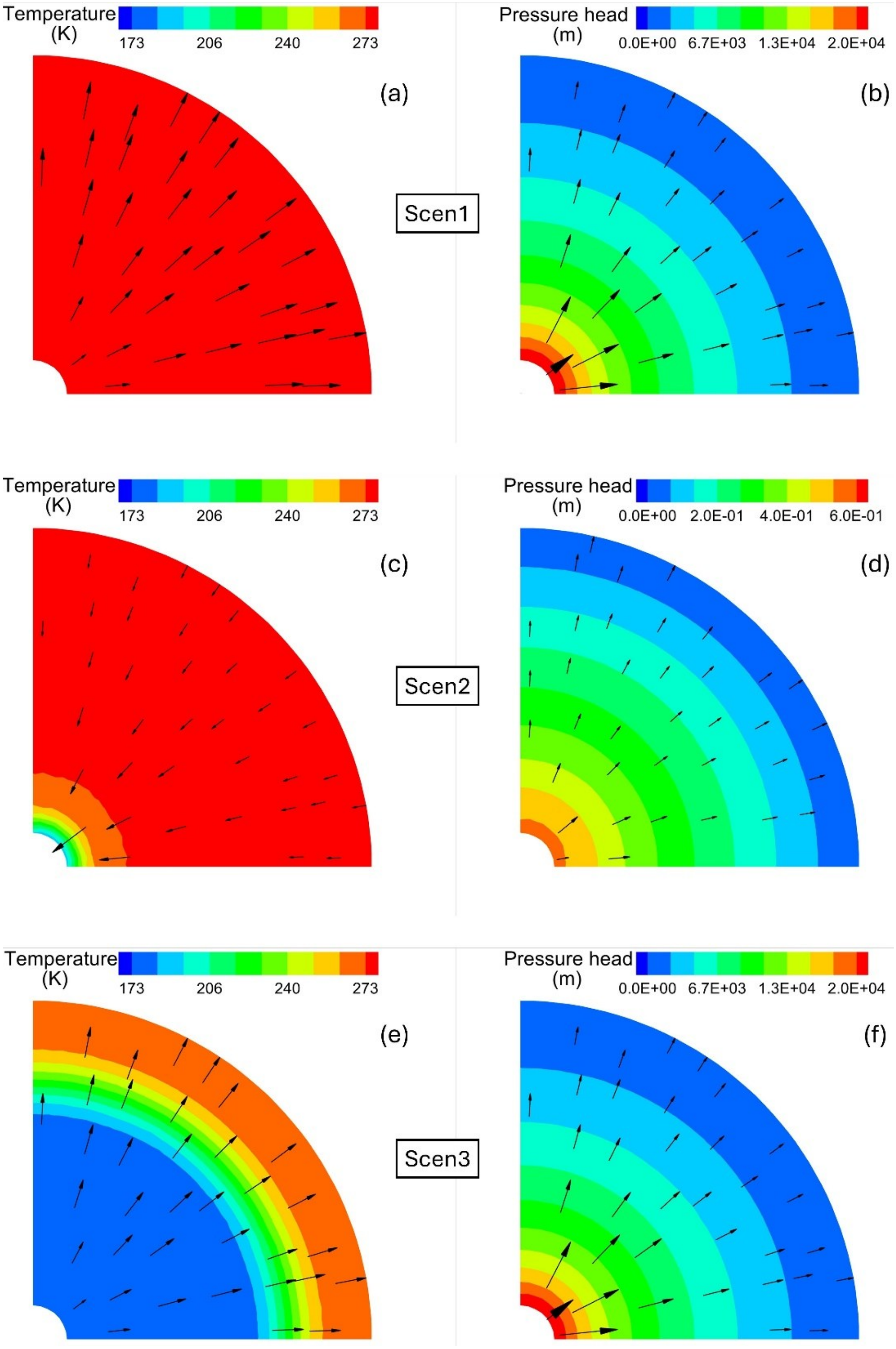

Figure 8: Results for the cold-water injection well problem at $t = 2\times10^4 \mathrm{s}$. Temperature distribution and displacement field for scenario 1 (a), scenario 2 (c), and scenario 3 (e). Pressure distribution and Darcy velocity field for scenario 1 (b), scenario 2 (d), and scenario 3 (f).

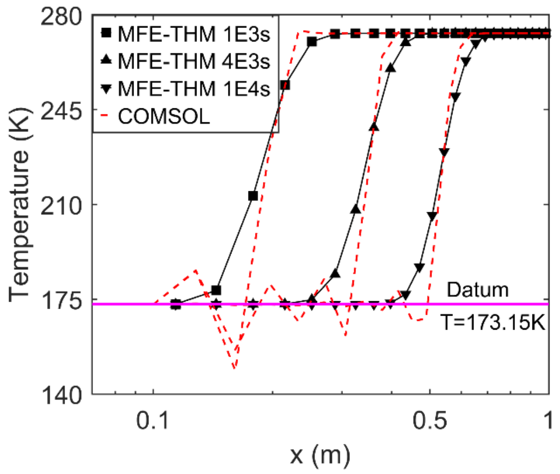

Figure 9: Temperature profiles at $y = 0$ m at different times for the cold-water injection problem.

Simulations for the scenario 3 are performed with the developed MFE-THM model as well as with COMSOL using the same mesh and iterative solver. Fig. 9 depicts the temperature profiles at $y = 0$ m for different steps in the case of a small effective thermal conductivity value $k^T = 0.2$ w/m/K to show the advance of the cold/hot temperature front during time. The results of COMSOL (based on the standard finite element method) show strong unphysical temperature oscillations (Fig. 9). The MFE-THM model avoids such instabilities and yields a monotonous temperature solution free of unphysical oscillations thanks to its advanced numerical scheme. To highlight the effect of the upwind technique used with the MFE method, two variants of the MFE-THM model (with and without upwind) are employed for the simulation of the current problem using different thermal conductivities k^T = 2.0/0.5/0.2 w/m/K. The obtained temperature distributions at $t = 4 \times 10^3 s$ are depicted in Fig. 10 for the different thermal conductivity values. In the case of large conduction heat transport with k^T = 2.0 w/m/K, both upwind and standard MFE schemes yield stable temperature distributions (Fig. 10a&d). However, in the case of moderate convection (k^T = 0.5 w/m/K) and in the case of convection-dominated heat transport (k^T = 0.2 w/m/K), the standard MFE method yields temperature distributions with strong unphysical oscillations, manifesting as extrema bands (Fig. 10b) and random spots (Fig. 10c) next to the cold temperature front. These oscillations are effectively removed when the upwind scheme is adopted (Fig. 10e&f). These results highlight the necessity of combining the MFE method with the upwind edge/face centered FV scheme technique for the solution of the convection-dominated heat transport problem.

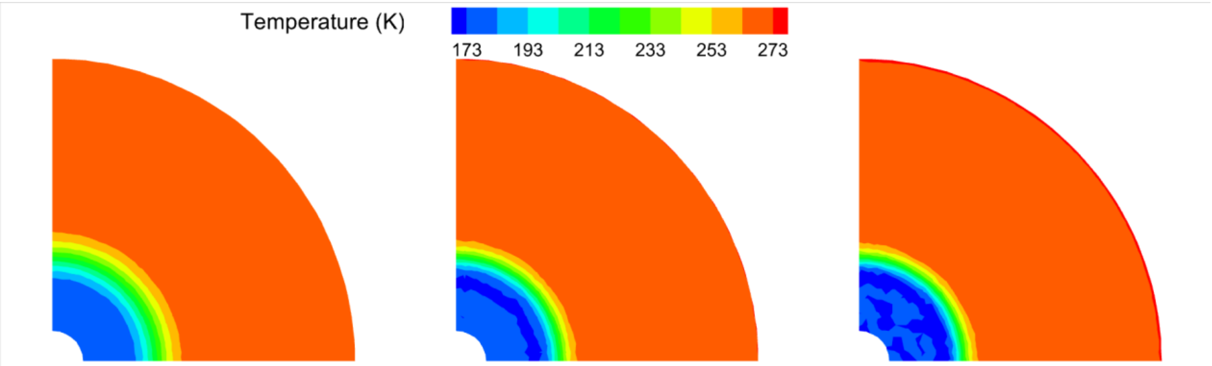

(a) k^T=2.0 Standard (b) k^T=0.5 Standard (c) k^T=0.2 Standard

(d) k^T=2.0 Upwind (e) k^T=0.5 Upwind (f) k^T=0.2 Upwind

Figure 10: Temperature distribution at $t = 4\times10^3 s$ using the MFE-THM model without (a,b,c) and with (d,e,f) the upwind technique using different thermal conductivity $k^T = 2.0/0.5/0.2$ for the cold-water injection problem.

4.3 Deformation of an unsaturated porous medium under partial surface load and hot water infiltration

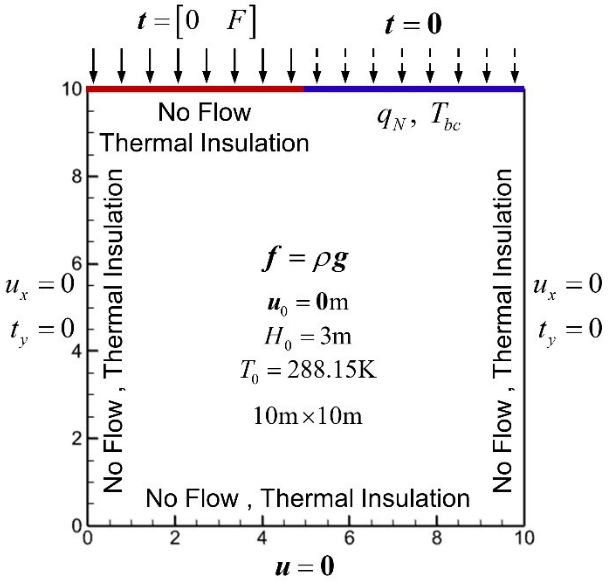

Figure 11: The configuration of an unsaturated porous medium under partial surface load and hot water infiltration.

Table 3: The material properties of the partially heat flux injection problem.

Parameter	Value
Water density ρ_w	1000 [kg/m^3]
Solid density ρ_s	2500 [kg/m^3]
Porosity n	0.3
Permeability k	1.0×10^{-11} [m^2]
Water compressibility C_w	2.0×10^{-10} [Pa^{-1}]
Solid grain compressibility C_s	1.1×10^{-7} [Pa^{-1}]
Water heat conductivity k_w^T	0.6 [w/m/K]
Solid heat conductivity k_s^T	0.9 [w/m/K]
Water heat capacity C_{Tw}	4200 [J/kg/K]
Solid heat capacity C_{Ts}	800 [J/kg/K]
Water volumetric thermal expansion coefficient α_w^T	6.0×10^{-4} [1/K]
Solid volumetric thermal expansion coefficient α_s^T	4.5×10^{-5} [1/K]
Young's modulus E	1.0×10^{7} [Pa]
Poisson ratio v	0.3
Biot's coefficient α	1.0

Saturated water content θ_s	0.3
Residual water content θ_r	0.01
Van Genuchten parameter α_v	2 [1/m]
Van Genuchten parameter n_v	2.05

This last test case deals with the THM problem under unsaturated conditions. The domain is a square porous medium of $10\mathrm{m}\times 10\mathrm{m}$ fixed in the bottom and normally constrained $\left(u^x = 0\right)$ in both left and right vertical sides (Fig. 11). A downward load $F = -10^5$ Pa is uniformly applied on the left half of the surface boundary. At the right-half surface boundary, water is injected with a constant flux $q_N = -8\times 10^{-6}\mathrm{m/s}$, and the temperature is fixed to $T_{bc} = 338.15\mathrm{K}$. The right half of the surface boundary is traction-free. All the other boundaries are thermally insulated and impermeable. The gravity is considered as a body force, $\boldsymbol{f} = \rho_b \boldsymbol{g}$ applied at $t = 0$. Initially, the porous material is assumed to be undeformed, with a uniformly distributed temperature of $T_0 = 288.15\mathrm{K}$ and a hydrostatic pressure distribution corresponding to an initial hydraulic head $H_0 = 3\mathrm{m}$. Thus, initially, the domain is saturated in its lower part and unsaturated in the upper part with a water table located at $y = 3\mathrm{m}$. The temperature interval for this problem is [288.15 338.15]K. The simulation of this problem is a challenging task because infiltration problems in initially dry soils often generate large head gradients at wetting fronts, which can cause unphysical oscillations and convergence issues (Zha et al., 2017). The problem is simulated for a duration of $3\times 10^5\mathrm{s}$ using the MFE-THM model on a triangular mesh of around 700 elements. At the end of the simulation, the domain is not fully saturated, and the upper left part of the domain remains unsaturated. The material properties for this problem are listed in Table 3.

In this problem, the surface boundary conditions for mechanics (prescribed load on the left half part), for hydraulic (fixed infiltration water flux on the right half part), and for heat (fixed temperature on the right half part), as well as the gravity body force impact the coupled THM process. Four different scenarios are simulated to show the impact of each single condition on the solution. In the first scenario, there is no load and no water infiltration at the surface. Further, the boundary temperature is chosen to be the same as that initially occurring in the domain $T_{bc} = T_0 = 288.15\mathrm{K}$. Hence, the porous medium is only subject to the gravity force $\boldsymbol{f} = \rho_b \boldsymbol{g}$, which is applied from $t = 0$. Fig.12a shows the obtained displacement field as well as the saturation distribution in the domain at $t = 3\times10^5\mathrm{s}$. At a given elevation, the same displacement is observed from the left to the right since the problem is mono-dimensional. The Fig.12b shows the initial vertical settlement profile at $x = 7\mathrm{m}$ (without gravity force) in blue, which is zero in the entire column, and the final vertical settlement profile at $t = 3\times10^5\mathrm{s}$ (caused by gravity) in red, which varies from zero at the fixed bottom, to its maximum value (around 6.4cm) near the surface. The Fig.12c shows the impact of the mechanics on the fluid flow. Indeed, the settlement caused by gravity, induces the water table level rise by approximately 19cm.

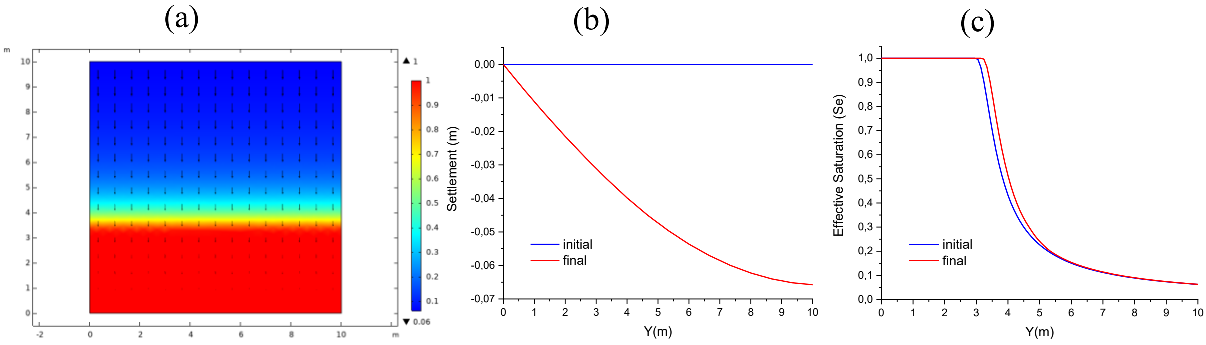

Figure 12: Results for scenario 1. Saturation distribution and displacement field (a), settlement profile at $x = 7\mathrm{m}$ (b) and saturation profile at $x = 7\mathrm{m}$ (c).

In the second scenario, the load is added to the left half part of the surface. As a consequence, the problem is no longer mono-dimensional and at a given elevation, the displacement increases from the right to the left (Fig.13a). The obtained displacement field is greater than that for the first scenario (Fig.13a). The settlement profile at $x = 7\mathrm{m}$ plotted in Fig.13b shows that the surface load increases the maximum settlement from 6.4cm to 7.9cm. Consequently, the saturation profile in Fig.13c shows that the water table level increases by approximately 28cm, which is 9cm more than previously.

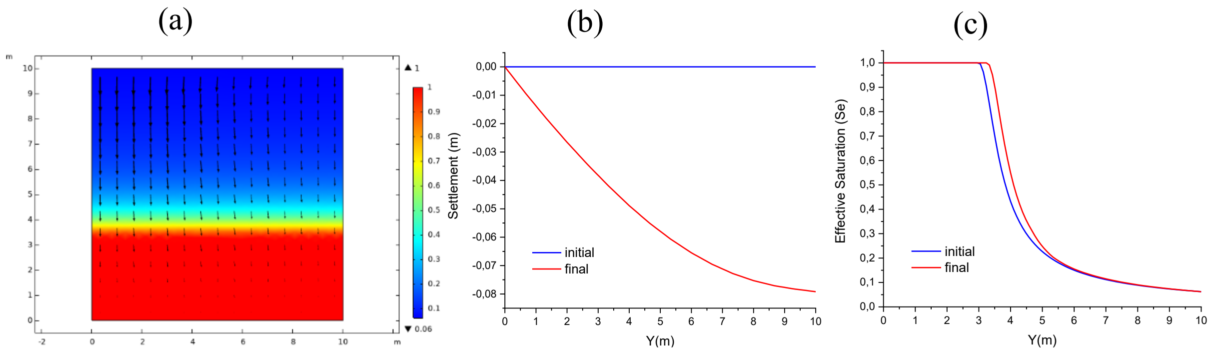

Figure 13: Results for scenario 2. Saturation distribution and displacement field (a), settlement profile at $x = 7\text{m}$ (b) and saturation profile at $x = 7\text{m}$ (c).

In the third scenario, in addition to the previous conditions, water is injected with a constant flux $q_N = -8 \times 10^{-6}$ m/s at the right-half part of the surface. Because of the water injection, the water table level rises until reaching approximately 7.6m at $t = 3 \times 10^5\text{s}$ (Fig.14a). The settlement profile at $x = 7\text{m}$ is plotted in Fig.14b for different time steps. The settlement varies with time due to the variable body force $\boldsymbol{f} = \rho_b \boldsymbol{g}$ in addition to the pore pressure change. Indeed, the bulk density $\rho_b = \rho_s (1-n) + nS_w \rho_w$ depends on the saturation, which varies with the water infiltration. Fig.14b shows that the settlement reduces as the porous medium becomes more saturated. Furthermore, the decrease of the settlement is not linear with time and is more pronounced as the domain becomes more saturated. For instance, between $t = 10^5\text{s}$ and $t = 2 \times 10^5\text{s}$, the maximum settlement reduces by 0.5cm (from 8.2cm to 7.7cm), whereas, it reduces by 1.1 cm (from 7.7cm to 6.6cm) between $2 \times 10^5\text{s}$ and $t = 3 \times 10^5\text{s}$. The saturation profile at $x = 7\text{m}$ is shown at $t = 0\text{s}$, $t = 1.5 \times 10^5\text{s}$ and $t = 3 \times 10^5\text{s}$ in Fig. 14c. Due to the continuous water injection, the water table level increases from its initial position (3m) to approximately 4m at $t = 1.5 \times 10^5\text{s}$ and to 7.6m at $t = 3 \times 10^5\text{s}$.

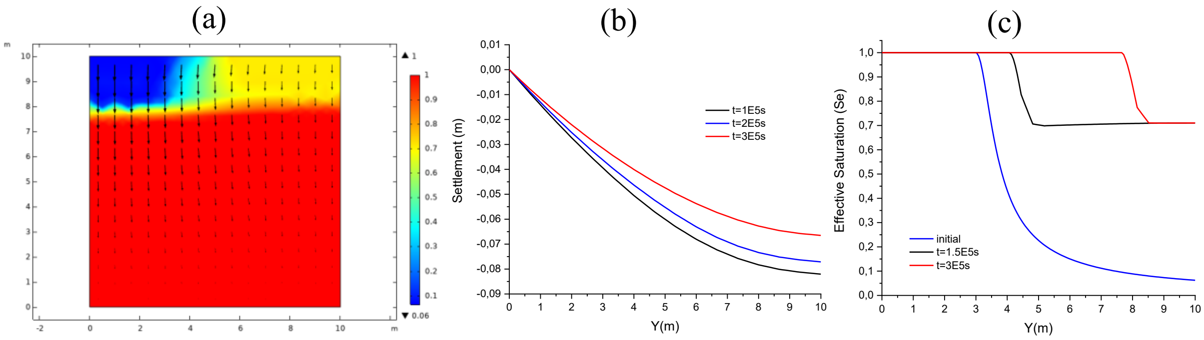

Figure 14: Results at $t = 3\times10^5\,\text{s}$ for scenario 3. Saturation distribution and displacement field (a), settlement profile at $x = 7\text{m}$ (b) and saturation profile at $x = 7\text{m}$ (c)

In the last scenario, we add heat transport from the surface by injecting hot water of $T_{bc} = 338.15\text{K}$ with $q_N = -8\times10^{-6}$ m/s from the right half surface. The temperature distribution at $t = 3\times10^5\,\text{s}$ in the domain as well as the displacement field are plotted in Fig.15a. The right upper corner is heated while the rest of the domain is still at the temperature $T_0 = 288.15\text{K}$. The temperature increase induces the dilation of the upper right region of the domain and, as a consequence, a reduction of the downward displacement in this region. Fig.15b shows the settlement profile at $x = 7\text{m}$ for $t = 1\times10^5\,\text{s}$, $t = 2\times10^5\,\text{s}$ and $t = 3\times10^5\,\text{s}$. In this figure, the red curve, corresponding to $t = 3\times10^5\,\text{s}$, is on the top, while the black one, corresponding to $t = 1\times10^5\,\text{s}$, is on the bottom. As shown in scenario 3, the settlement decreases with time since the domain becomes more saturated. Compared to scenario 3, the curves in Fig.15b have inflection points. The settlement increases from the bottom of the domain until reaching the heat front, then it starts to decrease because of the thermal dilation. The inflection points of the three curves in Fig.15b reveal the position of the heat front, which is around 8.5m at $t = 1\times10^5\,\text{s}$ and around 6.5m at $t = 3\times10^5\,\text{s}$. The final saturation distribution for scenario 4 is almost the same as that of scenario 3 (Fig.14c) since the fluid density and viscosity are considered constant, and their variation with temperature is neglected. In fact, a slight effect of the heat process on the hydraulic process exists through the mechanical process. Indeed, the reduction of the settlement, due to the hot temperature of the upper right region of the domain, induces a slight decrease in the water table level compared to scenario 3 (Fig.15c). This slight decrease in the water table level is mainly observable in Fig.15c at the end of the simulation when the heated region in the domain becomes large.

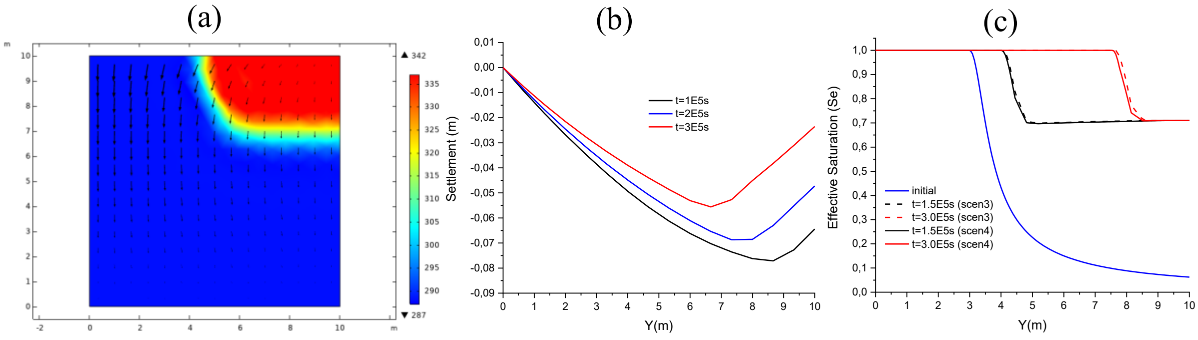

Figure 15: Results at $t = 3\times10^5$ s for scenario 4. Temperature distribution and displacement field (a), settlement profile at $x = 7$m (b) and saturation profile at $x = 7$m (c)

Robustness of the MFE-THM model

To show the robustness of the developed MFE-THM model for the simulation of thermo-poroelasticity problems in variably saturated media, the last scenario 4 is simulated with COMSOL multiphysics using the same coarse mesh formed by 700 elements and a finer mesh formed by 1900 elements and the obtained results (in terms of mechanics, hydraulic and heat) are compared to those obtained with the MFE-THM model on the coarse mesh.

For the mechanical results, COMSOL (using the coarse and the fine meshes) yields the same displacement field as the MFE-THM model using the coarse mesh (results not shown). For the hydraulic results, we plotted in Fig16a the saturation profiles on $x = 7$m at $t = 4\times10^4$s and $t = 10^5 s$ obtained from the MFE-THM model using the coarse mesh and COMSOL using the coarse and fine meshes to compare the performance of the three models. The COMSOL results on the coarse mesh show obvious local extrema reflecting unphysical oscillations near the wetting front for both investigated times. These unphysical oscillations are often observed with classical numerical methods when simulating the challenging problem of infiltration into initially dry soils due to the presence of sharp wetting fronts and are the origin of convergence problems and large computational costs (Zha et al., 2017). The mesh refinement with around three times more unknowns yields a strong reduction of these oscillations but cannot completely remove them. Contrarily, the results of the MFE-THM model on the coarse mesh (Fig.16a) are stable and free of oscillations.

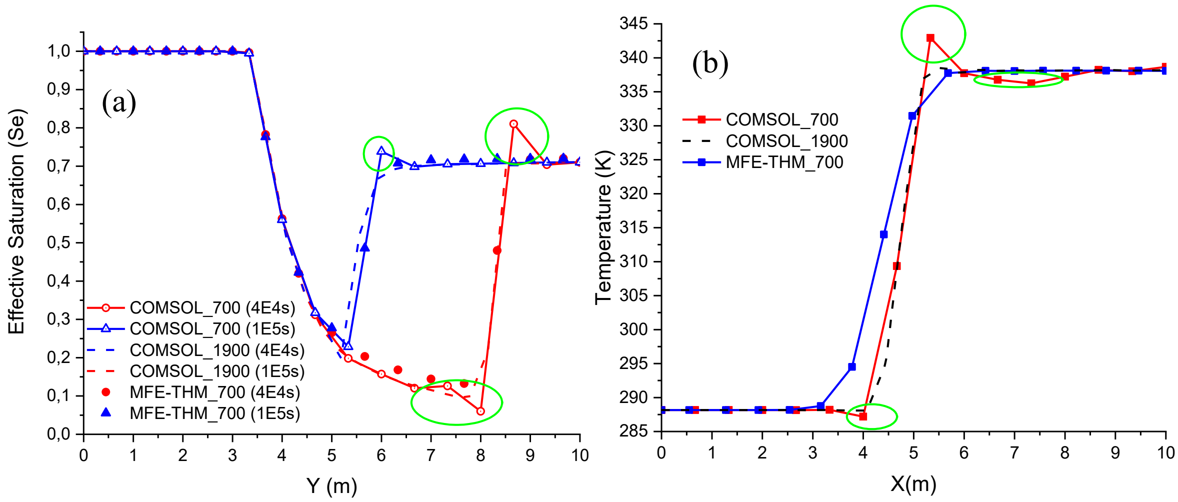

Figure 16: Results of MFE-THM (coarse mesh of 700 elements) and COMSOL (coarse mesh of 700 and fine mesh of 1900 elements) for scenario 4. (a) saturation profile on $x = 7\text{m}$ at $t = 4\times10^4\text{s}$ and $t = 10^5\text{s}$, and (b) temperature profile on $y = 9\text{m}$ at $t = 10^5\text{s}$.

Finally, to compare the heat results, the temperature profiles on $y = 9\text{m}$ obtained at $t = 10^5\text{s}$ are plotted in Fig. 16b. Since there is no sink/source term in the domain, the temperature everywhere should be between the initial temperature $T_0 = 288.15\text{K}$ and the boundary temperature $T_{bc} = 338.15\text{K}$. The results of COMSOL on the coarse mesh show spurious oscillations with local extrema near the sharp heat front (Fig.16b). The minimum and the maximum of the temperature profiles are given in Table 4 for COMSOL using the coarse mesh (700 elements) and the finer mesh (1900 elements) and for MFE-THM model using the coarse mesh. The results of this table show that COMSOL yields strong unphysical temperature oscillations with a maximum reaching 343K instead of 338.15K. These spurious oscillations diminish but remain when the mesh is refined (the maximum is 338.7K). The results of the MFE-THM model show a more diffusive front (because of the upwind procedure) but a more physical monotonous solution since all temperatures are between T_0 and T_{bc} (Table 4). On the other hand, these unphysical oscillations in the saturation and temperature solutions (Fig. 16) lead to serious convergence problems, which in turn increase the computational time. The average CPU time of the MFE-THM_700 model is 50s, whereas COMSOL_700 requires 185s because of the unphysical oscillations which preclude model convergence. For COMSOL_1900, the average CPU time increases drastically to 543s due to the mesh refinement. These results point out the efficiency and accuracy of the developed MFE-THM model for the simulation of the highly nonlinear thermo-poroelasticity problems in variably saturated domains.

Table 4: Maximum and minimum temperatures of the profiles on $y = 9\text{m}$ with COMSOL using a coarse mesh of 700 elements and a fine mesh of 1900 elements, and MFE-THM using the coarse mesh.

Simulator	$T_{\min}$	$T_{\max}$
COMSOL_700	287.19	343
COMSOL_1900	288.09	338.7
MFE-THM_700	288.15	338.15

5. CONCLUSIONS

The robust numerical simulation of thermo-poroelasticity problems in unsaturated porous media is challenging because of the high nonlinearity of the coupled processes and the nonphysical spurious oscillations in pressure, stress, and temperature solutions, which can lead to convergence problems and inaccurate results. In this work, a robust model is developed for the coupled THM processes in variably saturated domains using advanced numerical methods. Low-order numerical schemes are chosen to alleviate the computational burden. Due to its welldesired local mass conservation property, the MFE method is used for the fluid flow and heat transport in deformable unsaturated media. An upwind edge/face centered FV scheme is integrated with the MFE method for the heat transport solution to avoid the unphysical oscillations induced by the hyperbolic convection term. The nonconforming CR finite element method is used for the mechanics due to its locking-free and local mass conservation property. The developed MFE-THM model solves the coupled PDEs simultaneously using the monolithic scheme. The degrees of freedom are the hydraulic head, temperature, and displacement at the mesh edges. High-order time integration methods are employed for the time discretization, via the MOL. The order of the time integration and the size of the time step are adapted during the simulation to reduce the computational cost while maintaining accuracy.

Several numerical test cases are investigated to show the validation and the robustness of the new model. The first test case deals with the one-dimensional thermal consolidation problem and aims to validate the MFE-THM model for saturated thermo-poroelasticity problems. The pressure, temperature, and settlement solutions of the MFE-THM and COMSOL models at three observation points during the consolidation process show very good agreement with the analytical solution. Furthermore, mesh convergence analysis shows similar convergence rates with a slope around 2.0 for both MFE-THM and COMSOL models. The second test case concerns the deformation induced by the injection of cold water into a well. Simulation of this test case with the classical finite element method using COMSOL yields a temperature solution with strong unphysical oscillations. The MFE-THM model effectively avoids such instabilities in cases where convection dominates, thanks to the upwind edge/face centered FV scheme, integrated with the MFE method for the heat transport equation. The last test case deals with the deformation of a dry unsaturated porous medium under partial surface load and hot water injection. The effect of each boundary condition on the obtained displacement, saturation, and temperature distributions are investigated separately. The problem is simulated with COMSOL using a coarse mesh and a finer mesh containing three times more elements, and with the MFE-THM model using the same coarse mesh. The results of COMSOL using the coarse mesh show severe saturation oscillations near the wetting front, as well as significant temperature oscillations near the heating front. These spurious oscillations cause convergence problems and lead to a considerable increase of the computation time. Mesh refinement alleviates the unphysical oscillations in COMSOL solutions, but compromises the computational cost. The MFE-THM coarse mesh solution is in very good agreement with the fine-mesh COMSOL solution, but is less demanding in terms of computational cost and free from unphysical oscillations.

The performed numerical experiments have demonstrated the robustness and the high efficiency of the MFE-THM model. It should be noted that the efficiency of the developed model can be further improved by implementing high-performance computing techniques, in particular parallel algorithms.

The variably saturated condition in our model is a simplification of the two-phase flow scenario by assuming a quasi-static non-wetting phase. The developed model deserves to be extended to real two-phase or multiphase flow simulations, making it desirable for applications in CO2 sequestration and petroleum engineering, where high-pressure and high-temperature reservoir conditions are dominant. Finally, although this paper only investigated 2D THM problems in unsaturated porous media, the MFE-THM model can be easily extended to 3D problems using prismatic elements. Extending the model to 3D reservoirs and testing its computational performance is a valuable future work.

6. APPENDIX

The calculation of the matrices $\mathbf{C}_{HH}^T$, $\mathbf{C}_{TH}^T$, $\mathbf{C}_{MH}^T$, $\mathbf{C}_{TT}^T$, $\mathbf{C}_{MM}^T$, $\mathbf{C}_{HH}$, $\mathbf{C}_{TT}$, $\mathbf{C}_{HM}$, $\mathbf{C}_{TM}$, $\mathbf{C}_{MM}$, $\mathbf{Q}_\mathbf{f}$, $\mathbf{Q}_\mathbf{T}$, $\mathbf{Q}_\mathbf{m}$ are detailed as follows. The italic version of the symbols, C_{HH}^T , C_{TH}^T , C_{MH}^T , C_{TT}^T , C_{MM}^T , C_{HH} , C_{TT} , C_{HM} , C_{TM} , C_{MM} , Q_f , Q_T , Q_m represent the regular element in the corresponding matrices.

$$C_{HH}^T = -C_{pp}^E \frac{|E|}{3} - C_{pp}^{E'} \frac{|E'|}{3}$$

$$C_{TH}^T = C_{pT}^E \frac{|E|}{3} + C_{pT}^{E'} \frac{|E'|}{3}$$

$$C_{MH}^T = -C_{pe}^E \frac{\Delta y_i^E}{3} - C_{pe}^{E'} \frac{\Delta y_i^{E'}}{3}$$

$$C_{TT}^{T} = -\lambda_E - \lambda_{E'}$$

$$C_{HH} = \left\{ \frac{\alpha_{K,i}^{E}\alpha_{K,j}^{E}}{\alpha_{K}^{E}} - B_{K,ij}^{-1} \right\} + \left\{ \frac{\alpha_{K,i}^{E'}\alpha_{K,j}^{E'}}{\alpha_{K}^{E'}} - B_{K,ij}^{-1}{'} \right\}$$

$$C_{HT} = \left\{ -Q_{ij}^{E}\left(1-\tau_{ij}^{E}\right) \right\} + \left\{ -Q_{ij}^{E'}\left(1-\tau_{ij}^{E'}\right) \right\}$$

$$C_{TT} = \left\{ \frac{\alpha_{D,i}^{E}\alpha_{D,j}^{E}}{\alpha_{D}^{E}} - B_{D,ij}^{-1} \right\} + \left\{ \frac{\alpha_{D,i}^{E'}\alpha_{D,j}^{E'}}{\alpha_{D}^{E'}} - B_{D,ij}^{-1}{'} \right\}$$

$$C_{HM} = -\frac{\beta_p^{E}\Delta y_i^{E}}{3} - \frac{\beta_p^{E'}\Delta y_i^{E'}}{3}$$

$$C_{TM} = -\frac{\beta_T^{E}\Delta y_i^{E}}{3} - \frac{\beta_T^{E'}\Delta y_i^{E'}}{3}$$

$$C_{MM} = N_{E,ij}^{k},\ k = 1,2,3,4$$

$$Q_f = \frac{Q_s^{f,E}}{3} + \frac{Q_s^{f,E'}}{3}$$

$$Q_T = \frac{Q_s^{T,E}}{3} + \frac{Q_s^{T,E'}}{3}$$

$$Q_m = L_{\partial E_i} t_{\partial E_i}^{x}$$

7. REFERENCES

Antonietti, P.F., Bonetti, S., Botti, M., 2023. Discontinuous Galerkin Approximation of the Fully Coupled Thermo-poroelastic Problem. SIAM J. Sci. Comput. 45, A621–A645. https://doi.org/10.1137/22M1498747

Bai, B., 2005. One-dimensional thermal consolidation characteristics of geotechnical media under non-isothermal condition. Eng. Mech.

Belfort, B., Lehmann, F., Younes, A., Ackerer, P., 2010. A modified mass lumping procedure for the mixed hybrid finite element method applied to unsaturated water flow.

Belfort, B., Ramasomanana, F., Younes, A., Lehmann, F., 2009. An Efficient Lumped Mixed Hybrid Finite Element Formulation for Variably Saturated Groundwater Flow. Vadose Zone J. 8, 352–362. https://doi.org/10.2136/vzj2008.0108

Biot, M.A., 1941. General Theory of Three-Dimensional Consolidation. J. Appl. Phys. 12, 155–164. https://doi.org/10.1063/1.1712886

Boal, N., Gaspar, F.J., Lisbona, F., Vabishchevich, P., 2012. Finite-difference analysis for the linear thermoporoelasticity problem and its numerical resolution by multigrid methods. Math. Model. Anal. 17, 227–244. https://doi.org/10.3846/13926292.2012.662177

Both, J.W., Pop, I.S., Yotov, I., 2021. Global existence of weak solutions to unsaturated poroelasticity. ESAIM Math. Model. Numer. Anal. 55, 2849–2897. https://doi.org/10.1051/m2an/2021063

Brenan, K.E., Campbell, S.L., Petzold, L.R., 1996. Numerical Solution of Initial-value Problems in Differential-algebraic Equations. SIAM, New York.

Brezzi, F., Fortin, M., 1991. Mixed and hybrid finite element methods, Springer series in computational mathematics. Springer, New York Berlin Heidelberg. https://doi.org/10.1007/978-1-4612-3172-1

Brooks, A.N., Hughes, T.J.R., 1982. Streamline upwind/Petrov-Galerkin formulations for convection dominated flows with particular emphasis on the incompressible Navier-Stokes equations. Comput. Methods Appl. Mech. Eng. 32, 199–259. https://doi.org/10.1016/0045-7825(82)90071-8

Brooks, R.H., Corey, A.T., 1966. Properties of Porous Media Affecting Fluid Flow. J. Irrig. Drain. Div. 92, 61–88. https://doi.org/10.1061/JRCEA4.0000425

Brun, M.K., Ahmed, E., Berre, I., Nordbotten, J.M., Radu, F.A., 2020. Monolithic and splitting solution schemes for fully coupled quasi-static thermo-poroelasticity with nonlinear convective transport. Comput. Math. Appl. 80, 1964–1984. https://doi.org/10.1016/j.camwa.2020.08.022

Brun, M.K., Ahmed, E., Nordbotten, J.M., Radu, F.A., 2019. Well-posedness of the fully coupled quasi-static thermo-poroelastic equations with nonlinear convective transport. J. Math. Anal. Appl. 471, 239–266. https://doi.org/10.1016/j.jmaa.2018.10.074

Chavent, G., Roberts, J.E., 1991. A unified physical presentation of mixed, mixed-hybrid finite elements and standard finite difference approximations for the determination of velocities in waterflow problems. Adv. Water Resour. 14, 329–348. https://doi.org/10.1016/0309-1708(91)90020-O

Chen, Y., Ge, Z., 2022. Multiphysics Finite Element Method for Quasi-Static Thermo-Poroelasticity. J. Sci. Comput. 92, 43. https://doi.org/10.1007/s10915-022-01877-w

Dupray, F., Li, C., Laloui, L., 2013. THM coupling sensitivity analysis in geological nuclear waste storage. Eng. Geol. 163, 113–121. https://doi.org/10.1016/j.enggeo.2013.05.019

Gao, X., Li, T., Zhang, Y., Kong, X., Meng, N., 2022. A Review of Simulation Models of Heat Extraction for a Geothermal Reservoir in an Enhanced Geothermal System. Energies 15, 7148. https://doi.org/10.3390/en15197148

Gawin, D., Schrefler, B.A., Galindo, M., 1996. Thermo-hydro-mechanical analysis of partially saturated porous materials. Eng. Comput. 13, 113–143. https://doi.org/10.1108/02644409610151584

Guo, L., Younes, A., Fahs, M., Hoteit, H., 2024. An efficient fully Crouzeix-Raviart finite element model for coupled hydro-mechanical processes in variably saturated porous media. Adv. Water Resour. 186, 104663. https://doi.org/10.1016/j.advwatres.2024.104663

Hansbo, P., Larson, M.G., 2003. Discontinuous Galerkin and the Crouzeix–Raviart element: Application to elasticity. ESAIM Math. Model. Numer. Anal. 37, 63–72. https://doi.org/10.1051/m2an:2003020

Hindmarsh, A., 1982. Large ordinary differential equation systems and software. IEEE Control Syst. Mag. 2, 24–30. https://doi.org/10.1109/MCS.1982.1103756

Hu, M., Rutqvist, J., Wang, Y., 2017. A numerical manifold method model for analyzing fully coupled hydro-mechanical processes in porous rock masses with discrete fractures. Adv. Water Resour. 102, 111–126. https://doi.org/10.1016/j.advwatres.2017.02.007

Joseph Fourier, 1878. The analytical theory of heat. Cambridge [Eng.] : University Press.

Kafle, L., Xu, W.-J., Zeng, S.-Y., Nagel, T., 2022. A numerical investigation of slope stability influenced by the combined effects of reservoir water level fluctuations and precipitation: A case study of the Bianjiazhai landslide in China. Eng. Geol. 297, 106508. https://doi.org/10.1016/j.enggeo.2021.106508

Khoei, A.R., Moallemi, S., Haghighat, E., 2012. Thermo-hydro-mechanical modeling of impermeable discontinuity in saturated porous media with X-FEM technique. Eng. Fract. Mech. 96, 701–723. https://doi.org/10.1016/j.engfracmech.2012.10.003

Kim, J., 2018. Unconditionally stable sequential schemes for all-way coupled thermoporomechanics: Undrained-adiabatic and extended fixed-stress splits. Comput. Methods Appl. Mech. Eng. 341, 93–112. https://doi.org/10.1016/j.cma.2018.06.030

Kolesov, A.E., Vabishchevich, P.N., Vasilyeva, M.V., 2014. Splitting schemes for poroelasticity and thermoelasticity problems. Comput. Math. Appl., Efficient Algorithms for Large Scale Scientific Computations 67, 2185–2198. https://doi.org/10.1016/j.camwa.2014.02.005

Korsawe, J., Starke, G., 2005. A Least-Squares Mixed Finite Element Method for Biot's Consolidation Problem in Porous Media. SIAM J. Numer. Anal. 43, 318–339. https://doi.org/10.1137/S0036142903432929

Kraus, J., Lymbery, M., Osthues, K., Philo, F., 2024. Analysis of a family of time-continuous strongly conservative space-time finite element methods for the dynamic Biot model. https://doi.org/10.48550/arXiv.2401.04609

Kumar, S., Oyarzúa, R., Ruiz-Baier, R., Sandilya, R., 2020. Conservative discontinuous finite volume and mixed schemes for a new four-field formulation in poroelasticity. ESAIM Math. Model. Numer. Anal. 54, 273–299. https://doi.org/10.1051/m2an/2019063

Lee, S., Yi, S.-Y., 2022. Locking-Free and Locally-Conservative Enriched Galerkin Method for Poroelasticity. J. Sci. Comput. 94, 26. https://doi.org/10.1007/s10915-022-02079-0

Li, X., Cui, L., Roegiers, J.-C., 1999. Temperature Induced Pore Pressure And Stresses And Their Potential Impacts On Wellbore Stability. Presented at the 9th ISRM Congress, OnePetro.

Liu, R., Wheeler, M.F., Dawson, C.N., Dean, R., 2009. Modeling of convection-dominated thermoporomechanics problems using incomplete interior penalty Galerkin method. Comput. Methods Appl. Mech. Eng. 198, 912–919. https://doi.org/10.1016/j.cma.2008.11.012

Liu, Y., Yoshioka, K., You, T., Li, H., Zhang, F., 2024. A phase-field fracture model in thermo-poro-elastic media with micromechanical strain energy degradation. https://doi.org/10.48550/arXiv.2404.15322

Lu, Y., McCartney, J.S., 2024. Temperature effects on adsorption and capillarity water retention mechanisms in constrained unsaturated soils. Acta Geotech. 19, 6467–6482. https://doi.org/10.1007/s11440-024-02341-9

Menon, S., Song, X., 2023. Computational coupled large-deformation periporomechanics for dynamic failure and fracturing in variably saturated porous media. Int. J. Numer. Methods Eng. 124, 80–118. https://doi.org/10.1002/nme.7109

Mualem, Y., 1976. A new model for predicting the hydraulic conductivity of unsaturated porous media. Water Resour. Res. 12, 513–522. https://doi.org/10.1029/WR012i003p00513

Murad, M.A., Loula, A.F.D., 1994. On stability and convergence of finite element approximations of Biot's consolidation problem. Int. J. Numer. Methods Eng. 37, 645–667. https://doi.org/10.1002/nme.1620370407

Oyarzúa, R., Rhebergen, S., Solano, M., Zúñiga, P., 2021. Error analysis of a conforming and locking-free four-field formulation for the stationary Biot's model. ESAIM Math. Model. Numer. Anal. 55, S475–S506. https://doi.org/10.1051/m2an/2020045

Phillips, P.J., Wheeler, M.F., 2009. Overcoming the problem of locking in linear elasticity and poroelasticity: an heuristic approach. Comput. Geosci. 13, 5–12. https://doi.org/10.1007/s10596-008-9114-x

Phillips, P.J., Wheeler, M.F., 2008. A coupling of mixed and discontinuous Galerkin finite-element methods for poroelasticity. Comput. Geosci. 12, 417–435. https://doi.org/10.1007/s10596-008-9082-1

Phillips, P.J., Wheeler, M.F., 2007a. A coupling of mixed and continuous Galerkin finite element methods for poroelasticity I: the continuous in time case. Comput. Geosci. 11, 131–144. https://doi.org/10.1007/s10596-007-9045-y

Phillips, P.J., Wheeler, M.F., 2007b. A coupling of mixed and continuous Galerkin finite element methods for poroelasticity II: the discrete-in-time case. Comput. Geosci. 11, 145–158. https://doi.org/10.1007/s10596-007-9044-z

Raviart, P.A., Thomas, J.M., 1977. A mixed finite element method for 2-nd order elliptic problems, in: Galligani, I., Magenes, E. (Eds.), Mathematical Aspects of Finite Element

Methods, Lecture Notes in Mathematics. Springer, Berlin, Heidelberg, pp. 292–315. https://doi.org/10.1007/BFb0064470

Richards, L.A., 1931. Capillary conduction of liquids through porous mediums. Physics 1, 318–333. https://doi.org/10.1063/1.1745010

Ruiz-Baier, R., Lunati, I., 2016. Mixed finite element – discontinuous finite volume element discretization of a general class of multicontinuum models. J. Comput. Phys. 322, 666–688. https://doi.org/10.1016/j.jcp.2016.06.054

Rutqvist, J., Barr, D., Birkholzer, J.T., Fujisaki, K., Kolditz, O., Liu, Q.-S., Fujita, T., Wang, W., Zhang, C.-Y., 2009. A comparative simulation study of coupled THM processes and their effect on fractured rock permeability around nuclear waste repositories. Environ. Geol. 57, 1347–1360. https://doi.org/10.1007/s00254-008-1552-1

Song, X., Wang, K., Bate, B., 2018. A hierarchical thermo-hydro-plastic constitutive model for unsaturated soils and its numerical implementation. Int. J. Numer. Anal. Methods Geomech. 42, 1785–1805. https://doi.org/10.1002/nag.2811

Sun, M., Rui, H., 2017. A coupling of weak Galerkin and mixed finite element methods for poroelasticity. Comput. Math. Appl. 73, 804–823. https://doi.org/10.1016/j.camwa.2017.01.007

Taron, J., Elsworth, D., Min, K.-B., 2009. Numerical simulation of thermal-hydrologic-mechanical-chemical processes in deformable, fractured porous media. Int. J. Rock Mech. Min. Sci. 46, 842–854. https://doi.org/10.1016/j.ijrmms.2009.01.008

Tchonkova, M., Peters, J., Sture, S., 2008. A new mixed finite element method for poro-elasticity. Int. J. Numer. Anal. Methods Geomech. 32, 579–606. https://doi.org/10.1002/nag.630

Tocci, M.D., Kelley, C.T., Miller, C.T., 1997. Accurate and economical solution of the pressure-head form of Richards' equation by the method of lines. Adv. Water Resour. 20, 1–14. https://doi.org/10.1016/S0309-1708(96)00008-5

Van Genuchten, M.Th., 1980. A Closed-form Equation for Predicting the Hydraulic Conductivity of Unsaturated Soils. Soil Sci. Soc. Am. J. 44, 892–898. https://doi.org/10.2136/sssaj1980.03615995004400050002x

Vermeer, P.A., Verruijt, A., 1981. An accuracy condition for consolidation by finite elements. Int. J. Numer. Anal. Methods Geomech. 5, 1–14. https://doi.org/10.1002/nag.1610050103

Wang, K., Song, X., 2020. Strain localization in non-isothermal unsaturated porous media considering material heterogeneity with stabilized mixed finite elements. Comput. Methods Appl. Mech. Eng. 359, 112770. https://doi.org/10.1016/j.cma.2019.112770

Wang, Y., Papamichos, E., 1994. Conductive heat flow and thermally induced fluid flow around a well bore in a poroelastic medium. Water Resour. Res. 30, 3375–3384. https://doi.org/10.1029/94WR01774

Yi, S.Y., 2017. A Study of Two Modes of Locking in Poroelasticity. SIAM J. Numer. Anal. 55, 1915–1936. https://doi.org/10.1137/16M1056109

Yi, S.Y., 2014. Convergence analysis of a new mixed finite element method for Biot's consolidation model. Numer. Methods Partial Differ. Equ. 30, 1189–1210. https://doi.org/10.1002/num.21865

Yi, S.Y., 2013. A coupling of nonconforming and mixed finite element methods for Biot's consolidation model. Numer. Methods Partial Differ. Equ. 29, 1749–1777. https://doi.org/10.1002/num.21775

Younes, A., Ackerer, P., Delay, F., 2010. Mixed finite elements for solving 2-D diffusion-type equations. Rev. Geophys. 48. https://doi.org/10.1029/2008RG000277

Younes, A., Ackerer, P., Lehmann, F., 2006. A new mass lumping scheme for the mixed hybrid finite element method. Int. J. Numer. Methods Eng. 67, 89–107. https://doi.org/10.1002/nme.1628

Younes, A., Fontaine, V., 2008. Hybrid and multi-point formulations of the lowest-order mixed methods for Darcy's flow on triangles. Int. J. Numer. Methods Fluids 58, 1041–1062. https://doi.org/10.1002/fld.1785

Younes, A., Hoteit, H., Helmig, R., Fahs, M., 2022a. A robust upwind mixed hybrid finite element method for transport in variably saturated porous media. Hydrol. Earth Syst. Sci. 26, 5227–5239. https://doi.org/10.5194/hess-26-5227-2022

Younes, A., Koohbor, B., Belfort, B., Ackerer, P., Doummar, J., Fahs, M., 2022b. Modeling variable-density flow in saturated-unsaturated porous media: An advanced numerical model. Adv. Water Resour. 159, 104077. https://doi.org/10.1016/j.advwatres.2021.104077

Zareidarmiyan, A., Salarirad, H., Vilarrasa, V., Kim, K.-I., Lee, J., Min, K.-B., 2020. Comparison of numerical codes for coupled thermo-hydro-mechanical simulations of fractured media. J. Rock Mech. Geotech. Eng. 12, 850–865. https://doi.org/10.1016/j.jrmge.2019.12.016

Zha, Y., Yang, J., Yin, L., Zhang, Y., Zeng, W., Shi, L., 2017. A modified Picard iteration scheme for overcoming numerical difficulties of simulating infiltration into dry soil. J. Hydrol., Investigation of Coastal Aquifers 551, 56–69. https://doi.org/10.1016/j.jhydrol.2017.05.053

Zhang, J., Rui, H., 2024. A coupling of Galerkin and mixed finite element methods for the quasi-static thermo-poroelasticity with nonlinear convective transport. J. Comput. Appl. Math. 441, 115672. https://doi.org/10.1016/j.cam.2023.115672

Zhang, J., Zhou, C., Cao, Y., Meir, A.J., 2020. A locking free numerical approximation for quasilinear poroelasticity problems. Comput. Math. Appl. 80, 1538–1554. https://doi.org/10.1016/j.camwa.2020.07.011